

Contents lists available at ScienceDirect

Acta Materialia

journal homepage: www.elsevier.com/locate/actamat



Insights into the mechanism and kinetics of dissolution of aluminoborosilicate glasses in acidic media: Impact of high ionic field strength cations



Qianhui Qin^a, Nicholas Stone-Weiss^a, Tongyao Zhao^b, Pinaki Mukherjee^c, Jinjun Ren^b, John C. Mauro^d, Ashutosh Goel^{a,*}

- ^a Department of Materials Science and Engineering, Rutgers, The State University of New Jersey, Piscataway, NJ 08854, United States
- b Key Laboratory of Materials for High-Power Laser, Shanghai Institute of Optics and Fine Mechanics, Chinese Academy of Sciences, Shanghai 201800, China
- ^c Department of Materials Science and Engineering, Michigan Technological University, Houghton, MI 49931, United States
- d Department of Materials Science and Engineering, The Pennsylvania State University, University Park, PA 16802, United States

ARTICLE INFO

Article history: Received 12 July 2022 Revised 18 October 2022 Accepted 20 October 2022 Available online 23 October 2022

Keywords: Non-metallic glasses (silicates) Corrosion Structure-property relationship

ABSTRACT

Achieving thinner and higher performance display/substrate glasses and transparent glass-ceramics with tunable properties requires a precise control of acid-etching process, thus necessitating a comprehensive understanding of glass composition–structure–dissolution behavior relationships in acidic medium. Unfortunately, the literature on this subject has been focused only on a narrow set of glass chemistries. Therefore, consensus on the mechanisms that govern the acidic dissolution of multicomponent silicate glasses over a broad compositional space is still lacking. The present work employs a suite of state-of-the-art spectroscopic techniques, including 1D and 2D NMR, TEM-EELS, ICP-OES, and XPS, to provide an insight into the mechanism and kinetics of corrosion of alkali/alkaline-earth aluminoborosilicate glasses (comprising high field strength cations – HFSCs, i.e., La³+, Ti⁴+, Zr⁴+ and Nb⁵+) in acidic media (HCl; pH = 2). Incorporating the HFSCs into the glasses induces significant structural changes in their network, thus, impacting the forward rate dissolution kinetics. Based on the results, we hypothesize that the glasses dissolve at pH = 2 through an 'interfacial dissolution – re-precipitation mechanism (IDPM)' and 'in-situ recondensation' coupled pattern, wherein the IDPM results in a Si-rich alteration layer, followed by local recondensation occurring due to limited kinetics near the interfacial solution between the uncorroded glass surface and the outer alteration layer.

© 2022 Acta Materialia Inc. Published by Elsevier Ltd. All rights reserved.

1. Introduction

The fast-paced advancement in the field of portable electronics, micro-electromechanical system (MEMS) and photovoltaic devices has created a growing demand for thinner, higher performance display/substrate glasses and transparent glass-ceramics with tunable properties. This has prompted the development of novel processing techniques that can tune the properties of very thin glasses in a controllable manner. One such technique is the selective chemical etching of glass in acidic media that is being employed to create nanoscale features at the glass surface that can locally change the optical, mechanical, or even electrical properties of the glass without significantly altering its thickness. For in-

stance, Corning® has recently developed a novel coating-free antiglare borosilicate-based display glass by chemically etching out light-reflecting nanostructures on the glass' surface [1]. A similar method has also been applied to fabricate textured glass substrates that can be used as light guide plates in liquid crystal display (LCD) devices or exhibit reduced electrostatic charging during processing [2-4]. Additionally, it has been shown that the chemical etching of an alkali-free aluminoborosilicate glass (in acid) can modify the geometry of surface flaws resulting in a slow-down of crack propagation, thus, increasing the fracture toughness of the final product [5]. This advancement opens the avenue for the potential use of acid etching as a strengthening process for glassy materials that cannot be strengthened by chemical ion exchange. However, in each of the above examples, the targeted property depends directly on a precise control of the size and geometry of the resultant nanostructures; thus, the etching process must be performed in a highly controlled and well-predicted manner. Therefore, it is

^{*} Corresponding author. E-mail address: ag1179@soe.rutgers.edu (A. Goel).

crucial to have a comprehensive understanding of the fundamental science governing the corrosion of aluminoborosilicate glasses in acidic media—particularly relating to the impact of common constituent oxides. While several recent studies have aimed to unearth these relationships [6–15], a significant knowledge gap about the compositional dependence of chemical etching of glasses in acidic solutions still exists, as discussed below.

The literature about corrosion of glasses in acidic solutions approaches the problem from an academic perspective where the aim is to understand the mechanisms controlling the corrosion of silicate-, borosilicate-, and aluminosilicate-based glasses.[16-20] Though it provides a wealth of knowledge about the fundamental science of glass corrosion, it falls short of helping to resolve the technological challenges that are encountered during the processing (e.g., chemical etching) of functional glasses, owing to the compositional complexity of the latter. To put it in simple words: The majority of glass compositions reported in the literature are considerably simpler than advanced industrial glasses, comprising only one or two non-framework cations (for example, Na⁺ and Ca²⁺) along with a mixture of conventional network formers, i.e., SiO_2 , Al_2O_3 and B_2O_3 [16,18–21]. However, the chemical make-up of the technologically relevant glasses is significantly more complex, comprising multiple non-framework cations which, depending on their ionic field strength (IFS) may play varied roles resulting in a change in the degree of polymerization or introducing heterogeneity in the glass structure. As an example, ZrO₂ is usually added to functional glasses to increase their refractive index and/or mechanical strength, or to induce homogeneous nucleation of crystals. Nonetheless, owing to its high IFS $(Zr^{4+}: 0.77 \text{ Å}^{-2})$ [22], it induces several structural changes in the silicate glass structure which inadvertently alter the interaction between glass surface and the etchant [23,24]. Another example is that of Ti⁴⁺, which, either alone or in combination with Zr⁴⁺, is added to aluminosilicate glasses and melts to induce homogeneous crystallization [25-27]. Again, owing to its high IFS (Ti^{4+} : 1.04 Å⁻²) [22] along with its ability to exist in four-, five- and even six-coordination in the network, TiO₂ can induce several changes in the short-to-medium range order in the structure of silicate glasses, including affecting the degree of network connectivity by acting as an intermediate oxide, reducing the disorder around the alkali cations, and inducing phase separation [28-30]. All these changes in the structure of glasses are likely to affect the kinetics and mechanisms of interaction between the glass/glass-ceramic surface and the chemical etchant (mostly acidic). Unfortunately, our knowledge about the impact of these high field strength cations on the corrosion of multicomponent silicate glasses is limited primarily to only glasswater interactions. [14]. For example, when in contact with water, ZrO2 is known to increase the resistance of the glass against hydrolysis, owing to the increased network connectivity induced by Zr⁴⁺ ions. Nonetheless, ZrO₂ is also known to hinder the reconstruction of the altered layer towards passivation thereby resulting in a longer time required for the glass to enter the residual rate regime (Stage II), in which it dissolves in water at a much slower rate than in the forward rate regime (Stage I) [31]. Further complexity stems from the fact that Zr4+ can convert to higher coordination states in formed hydrated layers, which has been shown to depend on the pH and solution chemistry (i.e., saturated vs. undersaturated) of the surrounding environment [32,33]. Ti⁴⁺, on the other hand, is less effective in strengthening the glass network against hydrolysis, but, in the residual rate regime, allows gel layer reorganization to occur while also promoting the precipitation of secondary crystalline phases [9,20]. The exposure of multicomponent silicate glasses containing ZrO2 and/or TiO2 to acidic solutions is still an unknown territory that needs to be explored to not only help develop efficient industrial etching processes but also for the development of quantitative structure - property relationship (QSPR) models to predict the compositional and structural dependence of chemical durability of oxide glasses.

Accordingly, the work presented in this article focuses on understanding the impact of high field strength cations (La^{3+} , Ti^{4+} , Zr^{4+} , Nb^{5+}) on the dissolution behavior of alkali/alkaline earth aluminoborosilicate glasses in acidic solution (pH = 2). Table 1 presents the ionic radii and field strength of these cations. While the basis for selection of Ti^{4+} and Zr^{4+} in the present study has been discussed above, the choice of La^{3+} and Nb^{5+} has been made due to the following reasons:

- Rare-earth cations (RE³⁺), known for their high IFS (0.54 to 0.63 $Å^{-2}$ calculated based on the ionic radii data from Ref. [34]), are an integral component of several functional glasses, for example, nuclear waste glasses [35-37], optical glasses [38,39], and high modulus glasses [40]. The chemical durability is either an active or passive player in all of the above-mentioned applications, thus making it imperative to understand the impact (and fate) of RE3+ during the dissolution of these glasses. At the atomistic level, the structural role of rare-earth cations in borosilicate glasses is still debated. While one viewpoint suggests that RE³⁺ tend to cluster in peralkaline (Na/Al > 1) aluminoborosilicate glasses, thus, inducing nano-scale phase separation and leading to the segregation of borate-rich and silicaterich phases [41-44], the second viewpoint argues against the clustering tendency of rare-earth cations, instead suggesting the network modifying role of RE³⁺ in homogenous peralkaline aluminoborosilicate glasses [45,46]. These diverging viewpoints make the problem of establishing structure-durability relationships in rare-earth containing glasses intriguing and worth investigating. [47]. In this study, La³⁺ (IFS: 0.54 Å⁻²) has been used as a representative of rare-earth cations considering its diamagnetic nature that allows to probe the bulk structure of the pre- and post-corroded glass samples by nuclear magnetic resonance (NMR) spectroscopy.
- Nb₂O₅ is another technologically relevant oxide that is increasingly becoming an important component in the design and development of transparent glass-ceramics owing to the optical transparency of alkali niobate crystals (for example, LiNbO₃) [48,49]. Also, Nb₂O₅ is a well-known nucleating agent used to promote the crystallization of perovskite phases in piezoelectric glass-ceramics, [50] or to improve the thermal stability of glassy materials used as metal seals.[51,52] At the structural level, Nb^{5+} (IFS: 1.28 Å⁻²) is known to exist in four-, five- and six coordination in the structure of oxide glasses [53-58]. In silicate glasses, Nb⁵⁺ has been reported to incorporate into the silicate backbone as NbO₆⁻ octahedra in either of the two forms, i.e., a highly distorted type associated with non-bridging oxygens (NBOs) or a less distorted form without NBOs [53,56-58]. The complex configurations and role of Nb⁵⁺ in the structure of these glasses can affect their dissolution kinetics and behavior in unpredictable manner, thus, making it an interesting cation to investigate.

A total of five glasses with composition (100-x) $(12.5 \text{ Na}_2\text{O} - 12.5 \text{ CaO} - 5.0 \text{ Al}_2\text{O}_3 - 15.0 \text{ B}_2\text{O}_3 - 55.0 \text{ SiO}_2) - x\text{M}_x\text{O}_y$ (where, x = 0 and 5 mol.%; $\text{M}_x\text{O}_y = \text{La}_2\text{O}_3$, TiO_2 , ZrO_2 , Nb_2O_5) have been investigated for their dissolution behavior and kinetics in \sim 0.1 M HCl solution at pH_{25°C} = 2 \pm 0.01. A suite of state-of-the-art spectroscopic techniques have been employed to understand the structural and chemical evolution of the glasses (both in bulk and at surface) as a function of dissolution kinetics and the high field strength cation identity. The results from the present study will not only augment our current understanding of the fundamental science of glass corrosion but are expected to have tangible implications on the design of novel functional glasses with tailored surface topographies.

 Table 1

 Ionic field strength of some common cations in glass.

Element	Valance Z	Ionic Radius r (for CN = 6; Å)	Ionic Distance for Oxides a (Å)	Ionic Field Strength Z/a ²	Refs.
Na	1	0.98	2.30	0.19	[22]
Ca	2	1.06	2.48	0.33	[22]
La	3	1.03	2.35*	0.54	[34]
Zr	4	0.87	2.28	0.77	[22]
Ti	4	0.64	1.96	1.04	[22]
Nb	5	0.64	1.96*	1.30	[34]

^{*} Calculated from the reported ionic radius. $Z = r + r_{0^{2-}}$; $r_{0^{2-}} = 1.32$ Å from [22].

Table 2Batched and experimental (in brackets; measured via ICP-OES, ±0.5 mol%) composition (mol. %), T_g (°C) and density (g/cm³) of the studied glasses.

Sample ID	Batched Con	Batched Composition (mol. %)										
	Na ₂ O	CaO	Nb ₂ O ₅	ZrO ₂	TiO ₂	La ₂ O ₃	Al_2O_3	B ₂ O ₃	SiO ₂	T _g (°C)	Density (g/cm ³)	
BL	12.5[11.6]	12.5[13.4]	-	-	-	-	5.0[5.3]	15.0[13.9]	55.0[55.9]	605 ± 1	2.519 ± 0.002	
Nb-5	11.9[11.6]	11.9[12.9]	5.0[5.1]	-	-	-	4.8[4.9]	14.3[14.5]	52.3[51.0]	615 ± 2	2.730 ± 0.001	
Zr-5	11.9[10.2]	11.9[13.0]	-	5.0[5.2]	-	-	4.8[5.1]	14.3[14.1]	52.3[52.5]	626 ± 1	2.643 ± 0.002	
Ti-5	11.9[11.8]	11.9[12.8]	-	-	5.0[5.3]	-	4.8[4.9]	14.3[13.2]	52.3[52.0]	608 ± 2	2.561 ± 0.005	
La-5	11.9[10.6]	11.9[12.8]	-	-	-	5.0[5.2]	4.8[4.9]	14.3[15.0]	52.3[51.5]	$606 \pm 1;$	2.974 ± 0.005	
										718 ± 2		

2. Experimental

2.1. Glass synthesis

The glasses have been synthesized by a conventional meltquench technique using high purity powders of SiO₂ (Alfa Aesar; 99.5%), H₃BO₃ (Alfa Aesar; 98%), Na₂SiO₃ (Alfa Aesar; >99%), Al₂O₃ (Fisher Scientific; 99.7+%), CaCO₃ (Alfa Aesar; 98%), Nb₂O₅ (Strem Chemicals; 99.5%), ZrO₂ (Alfa Aesar; 99+%), TiO₂ (Fisher Scientific; >99%) and La₂O₃ (Fisher Scientific; 99.9%) as precursors. The compositions have been designed such that the molar ratio of constituent oxide remains same in all the glasses, thus enabling a direct comparison between the impact of different HFSCs on their structure and dissolution behavior. Batches yielding 150 g of glass were melted in Pt-Rh crucibles at 1575 °C for 1 h in ambient atmosphere and quenched on a copper plate. To minimize the residual stresses, the as-poured glasses were immediately transferred to a box furnace and annealed at $T_g^{\,*}$ – 50 °C for 1 h (where $T_g^{\,*}$ is the predicted glass transition temperature as obtained from the SciGlass database) [59]. The annealed samples were then analyzed by powder X-ray diffraction (XRD; PANalytical – X'Pert Pro; Cu K_{α} radiation; 2θ range: 10–90°; step size: 0.01313° s⁻¹) to confirm their amorphous nature. The experimental compositions were verified by inductively coupled plasma - optical emission spectroscopy (ICP-OES; PerkinElmer Optima 8300). The experimental glass transition temperatures (Tg) of the annealed samples were measured using differential scanning calorimetry (DSC; STA 449 F5 Jupiter®, Netzsch Inc.). The DSC measurements were performed at a heating rate of 20°C/min under a continuous N₂ flow (Pt pan, particle size of glass sample: < 45 $\mu m). The <math display="inline">T_g$ was deduced from the inflection point of the endothermic dip in the DSC spectra. The T_g value of each glass reported in the paper is an average of Tg values obtained from at least three DSC scans. Table 2 presents the batched and experimental compositions of the investigated glasses along with their measured Tg values.

2.2. Bulk structural analysis of glasses

²³Na, ²⁷Al, and ¹¹B magic-angle spinning nuclear magnetic resonance (MAS NMR) spectra of the annealed glasses (crushed to powder) were acquired on a Bruker Avance III HD 500 M spectrometer (4-mm Bruker MAS NMR probe) at 11.7 T. ¹¹B MAS NMR spectra (160.5 MHz resonance frequency) were obtained at a spinning speed of 10 kHz using RF pulses of 0.87 μs (15° tip angle)

with a recycle delay of 32 s. 27 Al MAS NMR spectra (130.4 MHz resonance frequency) were obtained at a spinning speed of 12 kHz using RF pulses of 0.56 µs (10° tip angle) with a recycle delay of 2 s. 23 Na MAS NMR spectra (132.4 MHz resonance frequency) were obtained at a spinning speed of 12 kHz using RF pulses of 1.4 µs (15° tip angle) with a recycle delay of 1 s. The acquired spectra for 11 B, 27 Al, and 23 Na were referenced to 1 M H $_3$ BO $_3$, 1 M Al(NO $_3$) $_3$ and 1 M NaCl solutions, respectively. All the spectra were fitted using DMFit software. [60]. To account for distributions in the quadrupolar coupling constants, 23 Na and 27 Al MAS NMR spectra were fitted by the CzSimple model. "Q MAS $\frac{1}{2}$ " and Gaus/Lor functions were used to fit 3- and 4-fold coordinated 11 B resonances, respectively, and N $_4$ (= $\frac{BO_4}{BO_3+BO_4}$) fraction was calculated from the relative areas of these peaks, with a small correction for the overlapping satellite transition of the 4-fold coordinated boron peak [61].

2.3. Sample preparation for corrosion tests

2.3.1. Glass powder specimens

Glass powders with particle diameter varying between 300 μm to 425 μm were obtained by crushing and sieving the annealed samples. To remove fine powder residue, the powders were ultrasonicated in acetone until the supernatant liquid was clear (typically ≥ 3 cycles). The ultrasonicated glass powders were dried overnight at room temperature in ambient air and analyzed using Fourier Transform Infrared (FTIR) spectroscopy to confirm the absence of any structural changes. The FTIR spectra were acquired using a single-bounce attenuated total reflectance (ATR) apparatus (FTIR-UATR, FrontierTM, Perkin Elmer Inc., diamond crystal, scanning resolution: 4 cm⁻¹, 32 scans for background and samples).

The geometric three-dimensional surface area of the acetone-washed glass particles was calculated using ImageJ software after capturing optical microscope images of \sim 1000 particles per composition at 50 × magnification (Zeiss Axioskop 40). A detailed methodology used to determine the surface area of powder specimens has been described in Ref. [62]. Using these values in combination with the experimental density values (measured using Archimedes' method by measuring mass of sample in air and in D-limonene solution; number of samples per composition = 3; standard deviation <0.005 g cm $^{-3}$; Table 2), the mean specific surface area of the washed powders was determined to be 3500-

4200 mm²/g. Finally, the mass of glass particles resulting in the desired surface area–to–solution volume ratio (S/V) was calculated.

2.3.2. Monolithic glass coupons

Based on the results of corrosion studies on powder samples, corrosion tests were performed on monolithic coupons of selected glass compositions. Two coupons with dimensions $\sim\!\!10~\text{mm}\times10~\text{mm}$ were cut for each glass composition using a diamond blade and polished according to the procedure described in ASTM C1220-10, [63] where the glass samples were ground in acetone sequentially using 120–600 grit sized SiC sheets followed by polishing in a 6 μm non-aqueous diamond suspension until a mirror finish was acquired. The thickness of the polished sample varied between 1 and 3 mm. The dimensions of the polished samples were measured to calculate the geometric surface areas.

2.4. Glass corrosion in acidic environments

2.4.1. Dissolution behavior and kinetics

The dissolution behavior of the glasses was studied under static conditions in $\sim\!0.1$ M HCl solution at pH₂₅ $^{\circ}C=2\pm0.01$ (experimental T = 65 °C; $S/V = 7.5 \text{ m}^{-1}$) in sterilized polypropylene flasks for duration varying between 1 h and 120 days without agitation. For each experiment, 95±0.1 mg of glass powder was added to 50±1 mL of freshly prepared acid solution. All experiments were performed in triplicate with a blank (glass-free) control to evaluate the uncertainty of the results. The evolution of solution pH was analyzed on recovered solution aliquots at room temperature using a pH meter (Mettler Toledo InLab® Pro-ISM). The solution aliquots from each experiment were analyzed for their elemental concentrations using ICP-OES (PerkinElmer Optima 8300). The ICP-OES detection limits were <0.5 ppm for Na, <0.2 ppm for Al, <0.2 ppm for B, <0.1 ppm for Si, <0.05 ppm for Ca, <0.08 ppm for Nb, <0.05 ppm for Zr, <0.03 ppm for Ti and <0.1 ppm for La. Each elemental concentration value reported in this paper represents an average of at least nine ICP-OES measurements (three aliquots for each sample, with each aliquot being measured thrice). The % fraction of alteration was calculated from the concentration of each constituent element in the solution using Eq. (1).

%Fraction of alteration_i =
$$\frac{(C_i - C_o)}{M \cdot f_i} \cdot V \cdot 100\%$$
 (1)

Further, the normalized loss (NL) of each element released into the surrounding solution was calculated using Eq. (2),

$$NL_i = \frac{C_i - C_o}{\left(\frac{S}{V}\right)f_i} \tag{2}$$

where C_i is the concentration (ppm-wt, or mg/L) of element i in the solution as detected by ICP-OES, C_o is the background concentration (as determined from the blank solutions), M is the mass of glass powder before dissolution (= 95±0.1 mg for all studied glasses), f_i is the mass fraction of the element i in the glass, and V is the volume of solution (= 50±1 mL). To compare the normalized release behavior of different elements and glass compositions, normalized loss data were plotted against time and the apparent linear regimes at early times were fitted with linear regression to estimate the forward rates.

Additionally, corrosion experiments were performed on polished monolithic glass coupons (prepared according to Section 2.3.2; two per composition) in identical conditions as the powder condition (pH = 2, 65°C; S/V = 7.5 m $^{-1}$) for 120-day durations. The glass coupons recovered after the dissolution experiments were rinsed thrice with deionized (DI) water, followed by rinsing in ethanol (Fisher Chemical, anhydrous) to remove any water sticking to their surface, and drying at room temperature.

2.4.2. Surface chemistry of pre- and post-corroded glasses

X-ray photoelectron spectroscopy (XPS) measurements were performed on both pre- and post-dissolution monolithic glass coupons to study the concentration and chemical environment of each element within the top 3-10 nm of surface layers. A Thermo Scientific K-Alpha instrument equipped with 1486.6 eV monochromated Al K_{α} X-ray source (to excite core level electrons from the sample) and a low energy dual electron/argon-ion beam flood gun for charge compensation was used for the XPS measurements. The kinetic energy of the photoelectrons was measured using a 180° double-focusing hemispherical analyzer with a 128-channel detector. Binding energies were referenced to the main component of the adventitious carbon peak at 284.8 eV. The photoelectron spectrometer was calibrated using the $Au4f_{7/2}$ binding energy (83.96 eV) for the etched surface of Au metal reference. The analyzer was operated in the constant resolution mode with a pass energy of 10 eV for high resolution spectroscopy, while a pass energy of 50 eV was used for the routine survey scans. Peak fitting for the core-level scans was performed using a mixed Gaussian-Lorentzian function (Gaussian: 85%) for obtaining binding energy and FWHM of the peaks. Peak areas were converted to composition using suitable elemental relative sensitivity factors [64] and corrected for attenuation through an adventitious carbonaceous overlayer using a calculation similar to the method described by Smith [65]. The probe depth of XPS, taken to be three times the inelastic mean free path of photoelectrons, was 3.6 nm for Na 1s, 9.0 nm for B 1s, 9.6 nm for Si 2p, 7.8 nm for Al 2p, 6.9 nm for O 1s, 8.1 nm for Nb 3d, 7.5 nm for Zr 3d, 7.2 nm for Ti 2p, 6.3 nm for La 3d and 11.4 nm for Ca 2p photoelectrons.

The hydrogen content on the surface of pre- and post-dissolution monolithic glass coupons was determined by electron recoil detection analysis (ERDA) using a 2.0 MeV He⁺⁺ beam (General Ionex Tandetron accelerator). The beam was oriented in a grazing geometry with an angle of 75° between the incident beam and the surface normal. The detector was mounted 75° with respect to the surface normal in the specular direction, with a 40 µm mylar foil placed over the active area to block scattered He ions. Hence, only forward-scattered H ions were able to penetrate the detector. The probe depth of reported ERDA data is approximately 300–400 nm.

2.4.3. Structural evolution in glasses as a function of aqueous corrosion

The glass powders retrieved after dissolution experiments (from Section 2.4.1) were subjected to the same washing and drying procedure as was performed for the corroded glass coupons. The recovered glass powders were analyzed by XRD, FTIR and ²³Na, ¹¹B and ²⁷Al MAS NMR spectroscopy. The experimental methodology and protocols for these characterization techniques have been discussed above.

Solid-state 27 Al{ 1 H} rotational-echo, double resonance nuclear magnetic resonance (REDOR NMR) spectra of the corroded glass powder were acquired on a Bruker Avance III-HD 500 NMR spectrometer (4 mm Bruker MAS NMR probe) at 11.7 T (spinning speed: 12 kHz) following the standard REDOR sequence published by Gullion and Schaefer [66]. The resonance frequency was 130.3 MHz and 500.1 MHz for 27 Al and 1 H, respectively, with a π REDOR pulse length of 5.6 μ s. Nine different echo times, $2\tau = NT_{\rm r} = 0.167, 0.333, 0.500, 0.667, 0.833, 1.00, 1.167, 1.333 and 1.500 ms, were employed to evaluate the <math>^{27}$ Al{ 1 H} effects of the corroded samples.

Solid-state 29 Si MAS NMR, 1 H MAS NMR and 1 H \rightarrow 29 Si cross-polarization (CP)-MAS NMR spectra of the corroded powder samples were recorded on a Bruker Avance III-HD 500 NMR spectrometer (4 mm Bruker MAS NMR probe) at 11.7 T. 29 Si MAS spectra (99.3 MHz resonance frequency) were obtained using

a 30° pulse of 2 μ s with a recycle delay of 300 s and a sample spinning speed of 6 kHz. 1 H MAS NMR (500.1 MHz resonance frequency) were measured using 90° pulse of 2.8 μ s with 1 s recycle delay at a spinning speed of 12 kHz. 1 H \rightarrow ²⁹Si CP-MAS NMR spectra were measured at a 2 ms CP pulse with a recycle delay of 2 s. Tetrakis(trimethylsilyl) silane and adamantane were used as the reference for ²⁹Si and 1 H chemical shift, respectively.

The chemistry and microstructure of the corroded glass particles was investigated using an FEI Titan Themis aberration corrected scanning transmission electron microscope (STEM) operated at 200 keV. Images of glass particles were obtained in scanning TEM modes with a point resolution of 0.8 Å. The microscope is fitted with an array of four windowless X-ray SuperXTM detectors for faster X-ray maps with better X-ray counts compared to conventional X-ray detectors [67]. For the present set of experiments, 20 µs dwell time and 100 pA beam current were used. The glass particles were firsthand ground for 2 min and suspended in methanol to make them electron transparent; they were then deposited on 200 mesh Cu grids covered with holey C film for TEM analysis. To identify any compositional changes occurring between the bulk and corroded layers, STEM-EDS (energy dispersive spectroscopy) was employed to measure the elemental distribution of the powder samples. Both the STEM and EDS data were acquired and analyzed using Thermo Fischer Velox software.

Since the EDS is insensitive to light elements (< Z = 11), Boron K-edge electron energy loss spectroscopy (EELS) was performed on the corroded glass particles using the Gatan Quantum GIF system. The convergence and collection semi-angles were 16.9 mrad and 12.8 mrad, respectively. All the obtained EELS spectra were calibrated using the O-K edge at 538 eV. Indexing and crystallographic calculations were performed using JEMS software.

3. Results

3.1. Glass formation

The as-synthesized glasses are transparent and X-ray amorphous after annealing below T_g^* (estimated using the SciGlass database) [59] for 1 h, as shown in Fig. S1. The DSC-measured T_g of the annealed glass samples are presented in Table 2. While the addition of Nb_2O_5 and ZrO_2 to the BL glass leads to a nonnegligible increase in the T_g value, the T_g values of glasses BL, La-5 and Ti-5 are all statistically similar. Further, the DSC thermograph of glass La-5 exhibits two endothermic dips before the crystallization curve representing two T_g values (Fig. S2), thus, suggesting the existence of glass-in-glass phase separation. The tendency of La_2O_3 (and other rare-earths) to induce nano-scale phase separation in alkali/alkaline-earth aluminoborosilicate glasses has been reported in our previous studies [37,44].

3.2. Structural analysis of annealed glasses

The 23 Na MAS NMR spectra of the studied glasses are presented in Fig. 1a, each displaying a broad asymmetric peak with maxima near -15 to -20 ppm. To better understand the Na environment and coordination in the annealed glass samples, all 23 Na MAS NMR spectra have been fitted using the CZSimple model in DMFit [60] and the optimized fitting parameters are presented in Table 3. While the addition of Ti⁴⁺, Zr⁴⁺, and Nb⁵⁺ to the BL glass leads to a slight upfield shift of the 23 Na $\delta^{\rm iso}$ (isotropic chemical shift; from -14.1 ppm for BL glass to -14.4, -14.9 and -15.4 ppm, respectively), La³⁺ substitution shifted the resonance in the opposite direction (to -12.8 ppm), highlighting the distinct effect of HFSC identity on the local Na environment in the glass structure. Since $\delta^{\rm iso}$ of the 23 Na resonance is negatively correlated to the average Na–O bond distance, $d({\rm Na-O})$, it is thus evident that the presence

of La³⁺ in the glass structure leads to a decrease in d(Na-0) while Ti⁴⁺, Zr⁴⁺, and Nb⁵⁺ additions increase d(Na-0). This distinction may be attributed to the effect that each HFSC has upon the glass structure. For instance, Ti⁴⁺, Zr⁴⁺ and Nb⁵⁺, when added in small amounts, typically incorporate into silicate-based glass structure as neutral or negatively charged polyhedra that require charge compensation by modifier cations (i.e. Na⁺ and/or Ca²⁺, in this case) [28,30,56,57,68–70]. They have also been observed to compete for charge-compensating cations with tetrahedral boron sites [68,71]. Due to these reasons, their presence thus results in a longer d(Na-0).

The downfield shift of the 23 Na 3iso in the glass La-5 is difficult to explain as the distinct structural role of La³⁺ (and RE³⁺, in general) in a multicomponent borosilicate glass is still debatable. The traditional viewpoint usually considers La³⁺ as a network modifier that behaves similar to Ca²⁺ (which is also a HFSC) in borosilicate and aluminosilicate glasses [45,46]. Therefore, the addition of La³⁺ to the glass will decrease the d(Na-O), assuming that La³⁺ randomly mixes with other non-framework cations such as Na⁺, and charge-compensate some of the AlO₄ an BO₄ units, thus, making more Na⁺ available to create NBOs in the glasse network. However, this does not seem to be the case in the glasses being investigated in the present study, as the presence of two glass transition temperatures in the DSC scan of glass La-5 is a clear evidence of phase separation (Fig. S2).

Another possible interpretation that would effect a shift in the role of Na⁺ is the so-called 'mixed cation effect,' as has been previously proposed in Na/Ca- and Na/Ca/La-containing glasses [46,72]. It has been hypothesized that because of their similar ionic radii (Na $^+$, 1.02 Å; Ca $^{2+}$, 0.99 Å; La $^{3+}$, 1.03 Å), these non-framework cations tend to pair up in the vicinity of NBOs and share the oxygen within their coordination shell to stabilize themselves. The literature reveals a good agreement between simulated and experimental ¹⁷O multiple quantum (MQ) MAS NMR spectra of Na₂O-CaO-La₂O₃-B₂O₃-SiO₂ based glass system assuming that each cation mixing site contains on an average 2.2 Na⁺ and 0.5 Ca²⁺ per La³⁺ [46]. In this way, the mixing cations become more 'network modifying' and a larger number of NBOs are required for charge-balancing. Here it should be noted that although Angeli et al. [46] did not report the clustering of La³⁺ in their glasses and instead defined the pairing of La³⁺ with Na⁺ and Ca²⁺ as "mixed cation effect," a recent spectroscopic study by Kamat et al. [44] on La³⁺/Nd³⁺-containing sodium aluminoborosilicate glasses proposes a similar model where La³⁺ requires charge compensation and tends to cluster when the surrounding environment is not sufficiently alkali-rich, causing the glass to undergo nanoscale phase separation into La-B-Na-rich (two to three Na⁺ per La³⁺) and Al-Si-rich phases. In our case, the DSC thermograph of glass La-5 (Fig. S2) does indicate the co-existence of two distinct phases suggesting nanoscale phase separation induced by the addition of La³⁺ to the glass. Nonetheless, from either viewpoint, it is evident that La³⁺ has a significant impact on the sodium environment in an alkali aluminoborosilicate glass.

Despite the difference in peak position, in all cases, the addition of HFSCs leads to insignificant change in quadrupolar coupling constant (C_Q), i.e., from 1.6 MHz in BL glass to 1.6-1.7 MHz in HFSC-containing glasses, suggesting similar distortion from local spherical symmetry around sodium ion in each of the investigated glasses [73].

The 27 Al MAS NMR spectra of the samples, as shown in Fig. 1b, display one broad peak centered around \sim 55 ppm, characteristic of tetrahedral Al (AlO₄ $^-$) units in silicate glass [15,19,74]. While 5- and 6-coordinated Al have been previously reported in silicate glasses containing HFSCs [45,73], these higher-coordinated species are not observed in the investigated glasses, as evidenced by the absence of distinct 27 Al NMR resonance around \sim 30 ppm or \sim 0

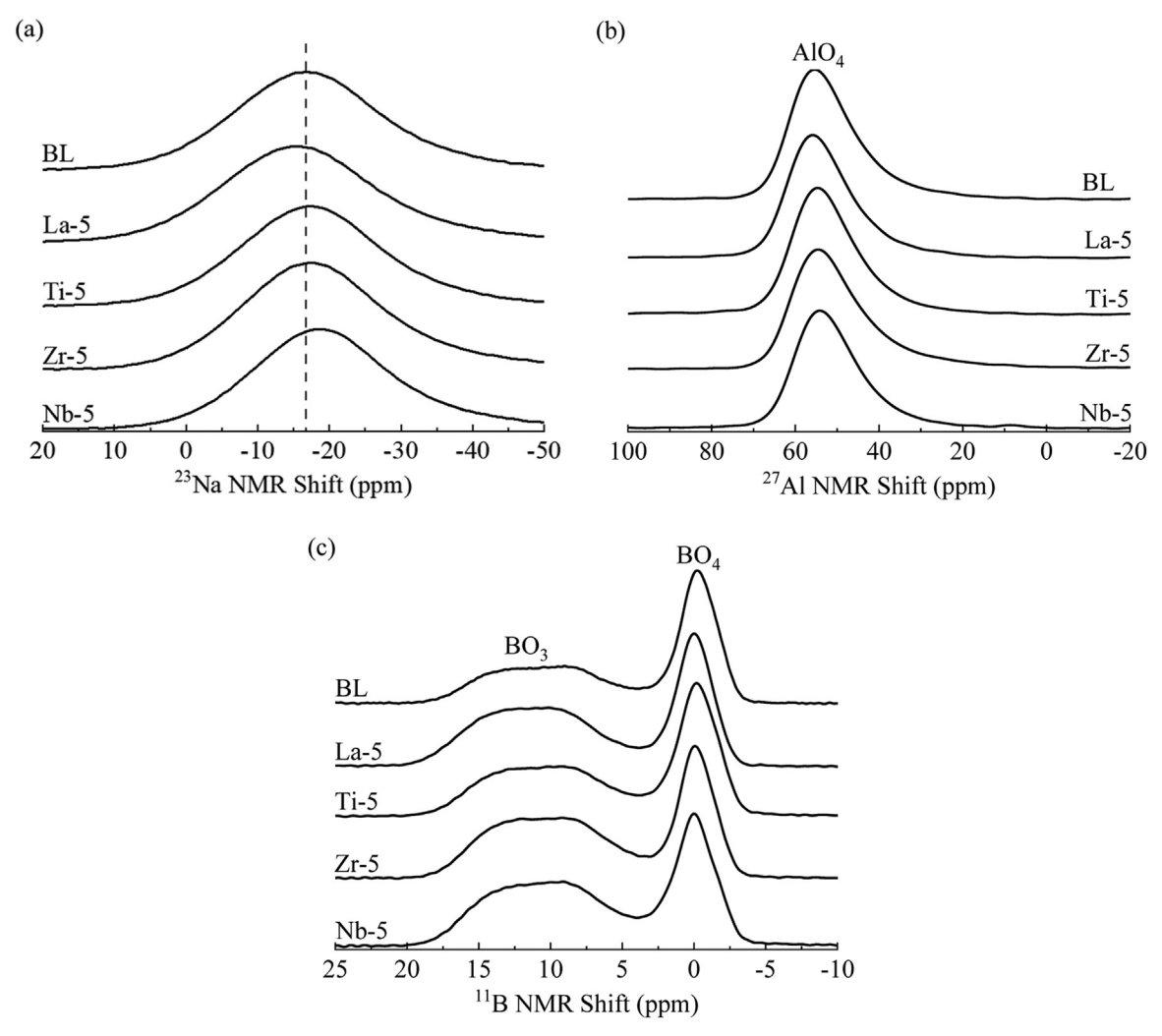


Fig. 1. (a) 23 Na, (b) 27 Al and (c) 11 B MAS NMR spectra of the as-prepared glass samples.

Table 3Average isotropic chemical shifts ($\delta^{iso}_{;\pm}$ ±0.5 ppm) and quadrupolar coupling constants (C_{Q} ; ±0.3 MHz) of fitted ²⁷Al and ²³Na MAS NMR data of the pre- and post-dissolution samples. Calculated N_4 fraction (±10%) and ring/non-ring BO₃ species ratio of the pre- and post-corroded glass samples, as extracted from ¹¹B MAS NMR

Sample ID	Duration	²³ Na MAS I	NMR	²⁷ Al MAS I	NMR	¹¹ B MAS NMR		
		δ^{iso}	$C_{\mathbb{Q}}$	δ^{iso}	CQ	N ₄	Ring/non-ring BO ₃ ratio	
BL	Pristine	-14.1	1.6	56.3	3.6	46.8	4.0	
	120 d	-11.9	1.6	57.5	3.2	41.8	3.1	
Nb-5	Pristine	-15.4	1.6	55.6	3.5	33.8	3.5	
	120 d	-15.4	1.6	56.1	3.5	33.0	3.7	
Zr-5	Pristine	-14.9	1.6	55.9	3.7	32.5	4.3	
	120 d	-14.2	1.6	57.1	3.6	31.9	4.3	
Ti-5	Pristine	-14.4	1.6	56.1	3.6	39.8	3.9	
	120 d	-14.3	1.6	57.2	3.5	37.9	3.8	
La-5	Pristine	-12.8	1.7	57.1	3.6	35.4	4.5	
	120 d	-12.5	1.7	56.8	3.3	35.4	5.0	

ppm [19,74], Fitting of the NMR spectra has been performed using the CZSimple model and has thus only considered the resonance from the tetrahedral Al units. The parameters extracted for these spectral fittings are listed in Table 3. It is observed that neither $\delta_{\rm iso}~(\pm 0.8~{\rm ppm})$ nor C $_{\rm Q}~(\pm 0.1~{\rm MHz})$ are significantly affected by the identity or field strength of the HFSC.

The 11 B MAS NMR spectra of all glass samples (Fig. 1c) exhibit two well-resolved peaks centered near 12 ppm and 0 ppm, corresponding to BO $_3$ and BO $_4$ units, respectively [75,76]. The BO $_3$ peak was fitted with two distinct components, attributed to ring-

and non-ring BO_3 units. Further, the BO_4 resonance was fitted adequately with two separate components following correction for the underlying satellite peak. The calculated fractions of each species are listed in Table 3. It is evident that while the addition of HFSCs does not exhibit a significant impact on the shape of the ^{11}B resonance, the relative area of the BO_3 resonance (N_3 ; the fraction of BO_3 species) increases significantly (+5.7-13.8%). It is well known that anionic BO_4^- units in glass must be charge-balanced by nearby non-framework cations, for example, N_4^+ and C_4^{2+} . Therefore, the boron speciation in a glass exhibits a strong dependence

on the amount and ionic field strength of the available chargecompensating cations [37,73,77,78]. As discussed above, Nb⁵⁺, Zr⁴⁺ and Ti⁴⁺ are known to form polyhedral units when incorporated into the silicate glass structure [28,30,56,57,68-70]. The ²³Na MAS NMR result also implies that in the studied glasses, the presence of the HFSCs shifts some Na+ from network-modifying to charge-compensating role. Since the molar ratios between other constituent oxides (i.e., between Na₂O, CaO, B₂O₃, Al₂O₃, and SiO₂) remain the same as the baseline glass after the addition of HF-SCs, the observed decrease in N₄ fraction can be readily explained by the preferential charge-compensation of HFSC structural units, thus, limiting the availability of charge compensators to the BO₄units. The determined N₄ fractions of the studied glasses (except La-5 glass, discussed later) follows the order: Zr-5<Nb-5<Ti-5<BL, which may correlate to differences in their valence and coordination environment in the glass. Both Nb^{5+} and Zr^{4+} cations have been shown to form octahedral units in the silicate glasses [56-58,68,69]. However, NbO₆ $^-$ requires less charge-compensation than ZrO_6^{2-} units, effecting a higher N_4 fraction in the Nbcontaining glass. Ti⁴⁺, on the other hand, can be present in both 4and 5-coordination (i.e., TiO₄ and TiO₅⁻, respectively) when added to silicate and aluminosilicate glasses in small amount (<5 mol%) [9,28,30,70,79]. TiO₄ does not require charge compensation, and it has been suggested that 5-fold Ti units do not show strong interaction with Na⁺ [80], both would account for the further increased N₄ fraction in the Ti-5 glass with respect to the Nb- and Zr-containing glass.

The lower N_4 value observed for the La_2O_3 -containing glass compared to that in BL, as also observed in the cases of Nb^{5+} , Zr^{4+} , and Ti^{4+} containing glasses, indicates that La^{3+} also competes with borate species for Na^+ , and such competition may be attributed to the prevalent mixing of Na^+ with La^{3+} in the borosilicate glass system. According to the literature [44,46], each La^{3+} would associate with two to three Na^+ to stabilize itself in the glass network, thus limiting the availability of Na^+ to BO_4^- species.

3.3. Dissolution behavior of glasses

3.3.1. Dissolution kinetics in HCl

The elemental NL curves, pH evolution and calculated fraction of alteration as a function of experiment duration are presented for each composition in Figs. 2, S3 and S4, respectively (Note: detailed pH readings, calculated NL values, and ICP-OES raw data are listed in Tables S1 and S2). The measured pH values maintain between 2.0 to 2.5 throughout the 120 days of experiment for all samples except the La-5 glass, in which the solution pH increases to $\sim\!2.75$ within 14 days of dissolution experiments and stabilizes at $\sim\!3$ as the reaction proceeds beyond 60 days. At the end of the 120-d experiments, all the studied compositions except La-5 glass have not reached complete dissolution (Fig. S4). For the glass La-5, the dissolution of all elements besides Si is calculated as near 100% during the 14- to 120-day period, merely leaving behind an Si-rich alteration surface.

3.3.1.1. Forward rate regime. The release of all the elements displays a linear trend with time during the first 3 h to 14 days of experiments, depending on the glass composition and kinetics of dissolution, corresponding to the forward rate regime commonly seen in the corrosion of silicate and borosilicate glasses. A few exceptions to this trend are the Na and Nb release from the glass Nb-5 and Zr release from the glass Zr-5, which each stay near or below the detection limit of ICP-OES within the forward rate regime. In the forward rate regime, the dissolution kinetics of silicate glasses depends on the hydrolysis of glass network, and thus, the glass composition and identity of network linkages. It should be noted here that an accurate picture of the forward rate in the

absence of flow-through conditions assumes an adequately dilute aqueous environment surrounding the glass with regard to the dissolved glass components. In the present study, we emphasize that a linear regression of this initial region represents an estimate of the forward rate and depicts a region in which solution feedback (i.e., dissolved silica) is not influencing non-linearity in elemental release from the glass. Accordingly, the fitted rates, as presented in Table 4, represent release of each constituent elements from the glasses when the solutions are less than ~33% saturated with regard to silica, i.e., the Si content in the solutions is \leq 33% of the estimated Si solubility limit in acid, as reported in Ref. [81]. The uncertainties listed in the table have been calculated from the uncertainty in the least-squares fitting method (discussed by Kragten [82]) using a similar approach as described in our previous publications. At the same time, uncertainties of 25% have also been considered while comparing rates, as has previously been assessed as a typical uncertainty attributed to rate determination in static experiments[83].

As evident from the fitted dissolution rates, for the BL glass (Fig. 2a) all elements except B and Si dissolve relatively congruently in HCl solutions following a regression of the first 3 days of experiments. While Si leaches out at a slightly slower rate from this glass compared to other constituent elements within the first 72 h, the release of B is much faster within the same duration. Similar results pertaining to a slow release of Si compared to boron from sodium borosilicate glasses in acidic solutions (HCl; pH <5) have been reported by Bunker et al., [84] and have been attributed to the high resistance of Si-O-Si bonds towards hydrolysis compared to B-O-B bonds. The introduction of Ti⁴⁺ to the BL glass effects a similar pattern of release, where all elements except Si are released congruently within the first 7 days (Fig. 2b), where Si is released at a slower rate. The addition of La³⁺, however, facilitates a much faster transition towards residual rate regime, as the NL curves of all constituent elements in the glass La-5 glass exhibit clear deviation from linearity after only 3 h of corrosion, therefore the reported forward rate is fitted using only (0,0) and 1-3 h data (Fig. 2c). In this glass, similar to the other glasses discussed above, all elements besides Si were released rapidly at similar rates within the first 3 h, while Si was released at a slower rate during the at same duration.

In contrast, it is observed that glass Zr-5 (Fig. 2d) features apparently congruent release of Na, Ca Al and, Si within 3 days of experiments, with slightly elevated boron release as compared to the other constituent elements. Since Zr release from the glass into the solution (in the initial 24 h of dissolution) is near or below the ICP-OES reporting limits, the forward rate of Zr could not be estimated. Nb-5 (displayed in Fig. 2e), on the other hand, exhibits congruent dissolution for all elements except Nb and Na within 14 days. For this glass, the amount of Nb in the solution remains below the detection limit of ICP-OES throughout the 120 days of experiment, while Na readings stabilize only after 14 days of immersion, as mentioned in the footnote of Table 4. As a result, the forward rate of Na and Nb is not reported for Nb-5 glass.

When comparing kinetics of glass dissolution as a function of the HFSC, while the addition of La³+ to the BL glass increases its forward dissolution rate by $\sim\!\!25\times$ (in terms of Na release), the addition of other three HFSCs, i.e., Nb⁵+, Zr⁴+ and Ti⁴+, results in slowed dissolution kinetics. For example, the glasses Nb-5, Zr-5 and Ti-5 exhibit a release rate of only $\sim\!\!0.1\times$ (based on Ca release), $\sim\!\!0.3\times$, and $\sim\!\!0.3\times$ (based on Na release), respectively, as compared to the BL glass. Here it should be noted that we have presented the results in terms of Na or Ca release from the glasses because these elements release from the glass at similar rates to other elements, thus allow an inter-glass composition comparison by forward rate trends.

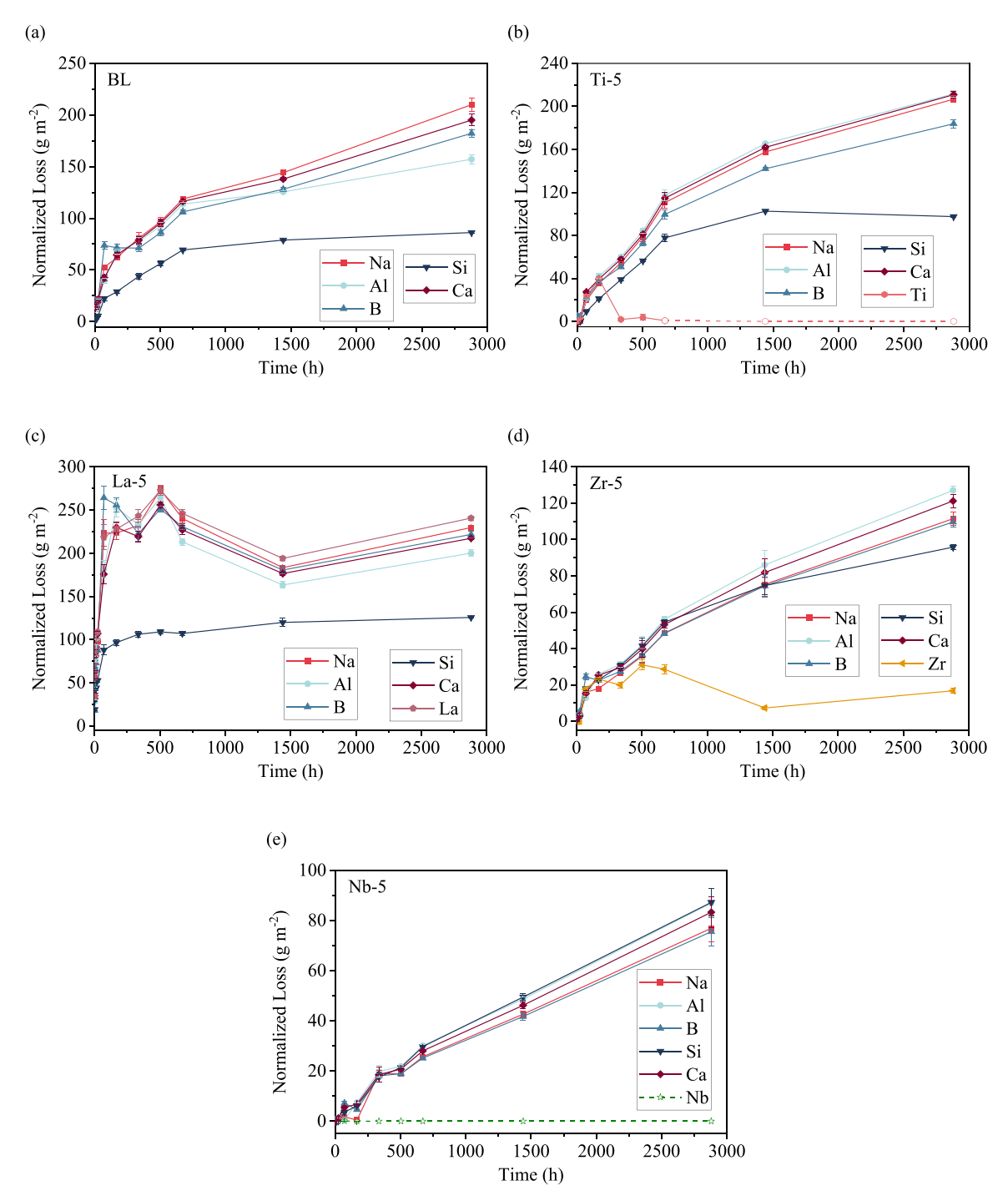


Fig. 2. Calculated elemental normalized loss as a function of time from glass: (a) BL, (b) La-5, (c) Ti-5, (d) Zr-5 and (e) Nb-5 in HCl solution. Each data point represents the average of three parallel experiments. Readings below detection limit of ICP-OES are marked with open symbols and dotted lines.

 $\label{eq:table 4} \textbf{Estimated forward rate } (g \cdot m^{-2} \ h^{-1}) \ \text{of the studied glasses for each constituent element.}$

Estimated F	Estimated Forward Rate									
Sample ID	Na	Al	В	Si	Ca	HFSC				
BL Nb-5 Zr-5 Ti-5 La-5	0.70±0.07 n.d.† 0.22±0.01 0.21±0.02 18±3	0.52 ± 0.09 0.059 ± 0.006 0.17 ± 0.01 0.26 ± 0.01 15 ± 4	$\begin{array}{c} 1.01{\pm}0.05 \\ 0.050{\pm}0.002 \\ 0.35{\pm}0.02 \\ 0.22{\pm}0.02 \\ 14{\pm}1 \end{array}$	0.32 ± 0.02 0.052 ± 0.004 0.26 ± 0.02 0.13 ± 0.01 9 ± 2	0.5±0.1 0.053±0.008 0.21±0.01 0.26±0.02 20±4	- Nb: n.d. [†] Zr: n.d. [†] Ti: 0.25±0.01 La: 20±4				

 $^{^{\}dagger}$ Not determined as the concentration of Na, Nb and Zr in the noted solutions was too low to be reported within the experimental uncertainty in the defined forward rate regime.

The observed variation in the corrosion kinetics upon the addition of different HFSCs can be explained based on the impact that different HFSCs exert on the glass network. Nb⁵⁺, Zr⁴⁺ and Ti⁴⁺, due to their high ionic field-strengths, can be present in the glass in various polyhedral forms with/without NBOs, and therefore do not strictly follow the traditional definition of 'networkformer'. However, their ability to intercalate into the glass network [30,56,57,68,69] and form relatively more hydrolysis-resistant bonds with other framework moieties (e.g., Si-O-Zr, as compared to Si-O-Si), [9] support our consideration of them as 'network reticulating agents', which strengthen the glass structure and lead to the observed lower forward rate (compared to the BL glass). Specifically, in case of TiO₂ and ZrO₂-containing glasses, while both being Group IVB elements, Zr4+ leads to a more significant inhibition on the initial dissolution than Ti4+ when added to the aluminoborosilicate baseline glass. Similar results have been reported previously [9,24], and may be related to the difference in the coordination between Zr4+ and Ti4+ as they incorporate into the glass network. While Zr⁴⁺ commonly forms octahedral ZrO₆²⁻ units in borosilicate glass [33,68,69,85], most literature reports Ti⁴⁺ as 4and 5-coordination [28,30,70,79], which not only has less bonding but also require less charge compensation than ZrO₆²⁻. Therefore, more non-framework cations (in our case, Na⁺ and Ca²⁺) would be consumed as charge compensator by Zr⁴⁺ than Ti⁴⁺, leaving less of them as modifier (or charge compensating BO_4^-). This argument is supported by the ¹¹B MAS NMR results showing that though the addition of ZrO2 and TiO2 to the BL composition both results in a decrease in N₄ fraction (compared to the BL glass), the Ti-5 glass has higher N₄ fraction than the Zr-5 glass. The higher measured Tg also implies a potentially stronger and denser bonding in the Zr-5 glass as compared to the Ti-5 glass. It can thus be inferred that Ti-5 glass has a less rigid network than the Zr-5 glass (but still higher network connectivity than the BL glass), accounting for the faster initial dissolution of the former. Nonetheless, the even more slowed initial dissolution kinetics observed in the Nb-5 glass (as compared to Zr-5 glass) cannot be explained by the same argument, as Nb⁵⁺ has also been widely reported to form octahedral units in silicate glass [56-58]. Therefore, we hypothesize that the slower dissolution kinetics of Nb₂O₅-containing glass may be related to the stronger interaction of Nb5+ with the surrounding oxygens due to its significantly higher ionic field strength than Zr4+ (Table 1) [86]. The much lower aqueous solubility as well as the higher free energy of formation of Nb₂O₅ [87-89] as compared to quartz and vitreous silica [90] also suggests a potentially higher resistance of Nb-5 glass against hydrolysis due to the formation of potentially hydrolysis resistant Si-O-Nb as compared to the Si-O-Si linkages. Further detailed investigations pertaining to glass-acid or glass-water interactions are warranted to validate the proposed

In contrast, the significantly faster initial dissolution of the Lacontaining glass is consistent with the structural model proposed in the literature suggesting that La³+ induces nanoscale phase separation in the glass [44]. The presence of multiple glassy phases, as apparent from two $T_{\rm g}$ values in the DSC, supports the argument that we are observing a faster dissolution of the more soluble phase rich in Na, La and B, thus making the La-5 glass appear more susceptible to acidic attack in comparison to the other glasses, especially in the forward rate regime.

It is observed in the ZrO_2 - and Nb_2O_5 -containing glasses that the elemental NL value continues to increase in a relatively linear manner after the initial 3-14 days of corrosion (Fig. 2d and e), and no clear residual rate plateau can be observed throughout the 120-day duration of experiments. Considering the slow corrosion kinetics of these glasses, presumably they are still in a stage of slow transition towards the residual rate regime at the end of the experiment. Thus, in the next section, we will

mainly focus on the residual rate behavior in the remaining glasses.

3.3.1.2. Residual rate regime. As shown in Fig. 2a, the dissolution kinetics of glass BL slow down after 72 h followed by a transition into residual rate regime after 28 days. During the residual rate regime, boron continues to dissolve congruently with Na, Ca, and Al, while the release of Si further deviates from congruency. The addition of TiO₂ to the BL glass did not exhibit a significant impact on its dissolution kinetics in the residual rate regime, as evident from Fig. 2b, except that the NL of Ti drops below the detection limit of the ICP-OES after 14 days of corrosion. The glass La-5, owing to its significantly faster kinetics of dissolution (compared to glass BL) in the forward rate regime, transitions into the residual rate regime after 72 h, where all the elements except Si are released congruently into the solution (Fig. 2c). As compared to the BL glass, which presents a much slower but non-zero residual rate at the end of experiment, the passivation effect is apparently more efficient in the La-containing sample (considering the fast initial dissolution kinetics of La-5 glass), as evident from the comparable NL_{Na} values of glasses BL (\sim 210 g/m²) and La-5 (\sim 230 g/m²) after 120 days. The ZrO2-containing glass shows a dissolution behavior similar to that observed in TiO2-containing glass, wherein the Zr concentration in the solution drops below the detection limit of the ICP-OES after 28 days (Fig. 2d). The drastic decrease in the NL values of Ti and Zr after 14 and 28 days, respectively, may be attributed to the low solubility of Ti⁴⁺ and Zr⁴⁺ in dilute HCl [91,92], which causes their precipitation onto the surface of glass. The delay in the precipitation of Zr (28 days compared to 14 days for Ti in Ti-5 glass) may be attributed to the slower dissolution kinetics of ZrO₂-containing glass. In fact, as mentioned in Section 3.2.1.2, due to their slower kinetics of dissolution, the Zr-5 and Nb-5 glasses appear to be still in the stage of a gradual transition towards residual rate regime at the end of the experiments. Therefore, it is not feasible to discuss their residual rate behavior herein. Nevertheless, the addition of ZrO2 and Nb2O5 to the BL glass leads to a much lower final NL_{Na} value (\sim 111 and 77 g/m², respectively), indicating the inhibiting effect of Zr⁴⁺ and Nb⁵⁺ against acidic corrosion within the timescale of our experiments.

3.3.2. Structural characterization of corroded powders

The XRD patterns of all pre- and post-dissolution samples are presented in Fig. S1. All the glass powders (except Ti-5) are XRD amorphous until 120 days of corrosion in HCl. The XRD patterns of glass Ti-5 reveal the presence of crystalline peaks likely corresponding to anatase, a tetragonal polymorph of TiO₂, after 28 days and 120 days of corrosion in HCl (Fig. S5). Although the precipitation of Zr and Nb-related phases is also expected in Zr-5 and Nb-5 glass-solution mixtures, no signs of crystallinity are evident from the XRD patterns of post-dissolution glass powders from these samples. The formation of crystalline TiO₂ in the Ti-5 sample can be explained based on the faster dissolution kinetics of Ti-5 glass (compared to Zr-5 and Nb-5), which leads to the local supersaturation of Ti near the glass surface followed by rapid nucleation and growth of solid phase into a crystalline product. It should be noted here that nucleation does not necessarily begins on reaching the supersaturated condition, except at a very high supersaturation, and there may be an induction period before the detection of first crystal or solid particle. Thus, the absence of any crystalline products in the precipitates of Zr-5 and Nb-5 samples may be attributed to the lower degree of supersaturation (due to their slower dissolution kinetics), which results in an induction period before the detection of any crystalline phases.

While the XRD data of the post-dissolution glass powders did not show any signs of crystallinity (except in Ti-5 sample), a comparison of the FTIR-ATR spectra of the pre- and post-dissolution

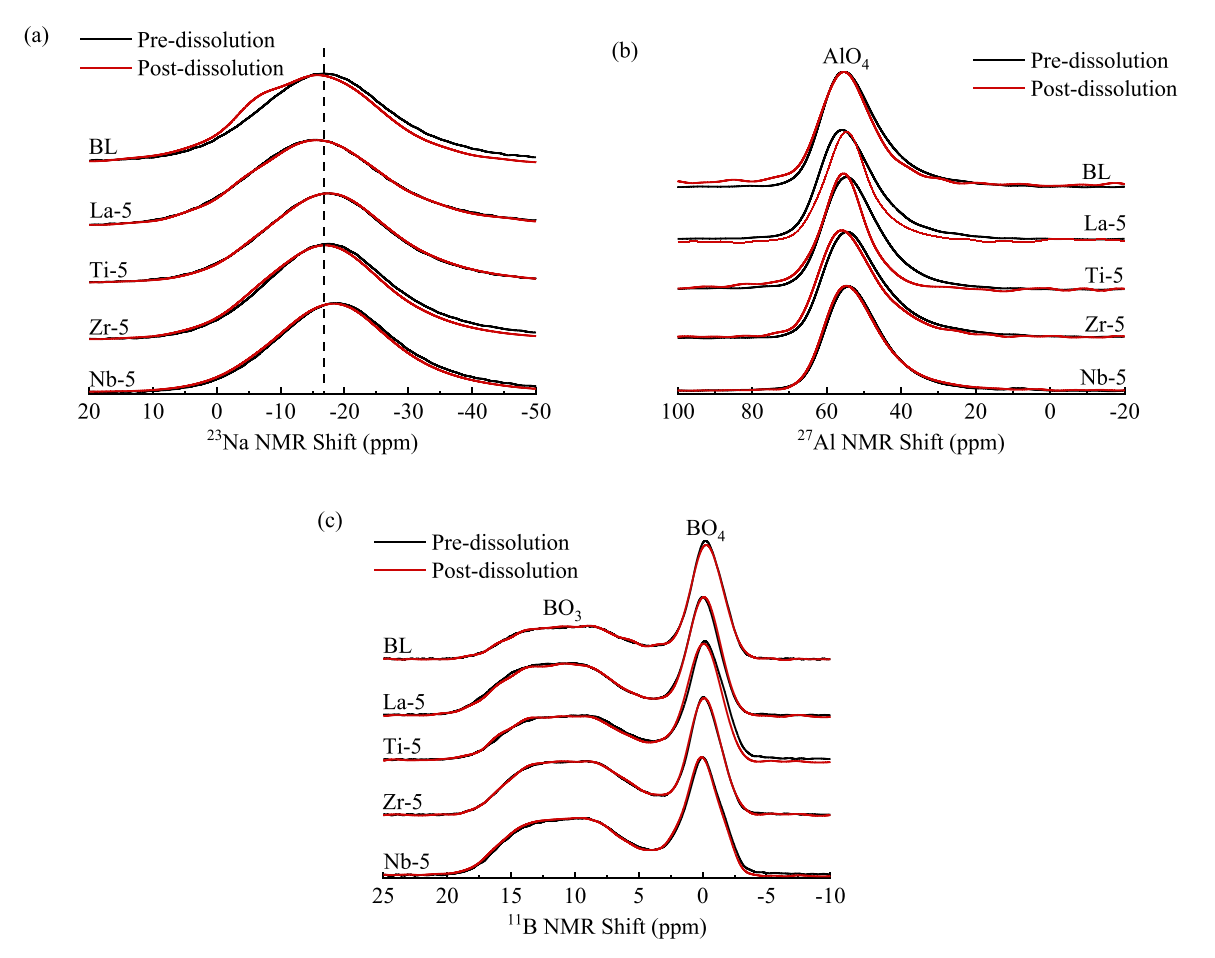


Fig. 3. (a) 23 Na, (b) 27 Al and (c) 11 B MAS NMR spectra of the 120-day corroded samples. 23 Na, 27 Al and 11 B MAS NMR spectra measured on the un-corroded samples have been added for comparison.

powders (Fig. S6) reveals the formation of absorption bands at $\sim\!1635~\rm cm^{-1}$ and $\sim\!3390~\rm cm^{-1}$ in the samples after 120 days of corrosion, corresponding to the $\rm H_2O$ bending and OH stretching modes, respectively [6,8,93], thus suggesting the formation of hydrated layer(s). Additionally, the FTIR-ATR spectra of post-dissolution glass powders from compositions BL, Ti-5 and La-5 show a significant weakening in the vibration modes of BO_3 units located at $\sim\!700~\rm cm^{-1}$ [94–96], which can be attributed to an extensive leaching of B species into the solution, as also suggested by the NL data.

In order to understand the structural evolution of glasses as a result of corrosion, 27 Al, 23 Na and 11 B MAS NMR analyses have been performed on glassy grains recovered after 120 days of dissolution experiments. Fig. 3a and b present the 23 Na and 27 Al MAS NMR spectra of the pre- and post-dissolution glass powders, respectively, while Table 3 presents the optimized fitting parameters for these spectra. As evident in Fig. 3a, for all the investigated glass compositions except BL, the 23 Na MAS NMR spectra of the corroded samples overlap closely with that of the uncorroded samples. For the BL glass, 23 Na spectra show a slight downfield shift (+2.2 ppm) after corrosion, indicating a decrease of d(Na-O).

The ²⁷Al MAS NMR spectra of the post-dissolution glass samples (Fig. 3b) comprise one broad peak around ~57 ppm corresponding to AlO₄⁻ units in the glass structure [15,19,74]. The ²⁷Al MAS NMR spectra of the post-dissolution glass powders does not suggest the possible presence of any higher-coordinated aluminum species. Nevertheless, the change in the ²⁷Al resonance shape can be observed for glasses BL, Ti-5 and La-5, marked by a general de-

crease in the C_Q value (-0.4, -0.1 and -0.3 MHz, respectively) and a slight shift in the fitted $\delta_{\rm iso}$ value (+1.2, +1.1 and -0.3 ppm, respectively, as listed in Table 3). Since C_Q value is a measure of the deviation from perfect cubic symmetry around the Al environment, these results, thus, suggest that the glass network of post-dissolution BL, Ti-5 and La-5 samples is less distorted around 4-coordinated Al species upon corrosion [97,98].

To identify the origin of change in the shape of ²⁷Al NMR spectra of glasses due to corrosion, the ²⁷Al{¹H} REDOR NMR analysis has been performed on the 120-day corroded Ti-5 glass (which shows the most significant change in ²⁷Al resonance upon corrosion). Fig. 4a displays the comparison between S₀ and S spectra at an echo time of 1.5 ms, where the extent of spectral dephasing is indicated by the difference curve. Further, Fig. 4b shows the REDOR curve of this sample, plotted as $\Delta \text{S}/\text{S}_0$ (spectral dephasing) vs. number of rotor cycles (dipolar mixing time), where increased curvature indicates a greater extent of ²⁷Al-¹H interaction in the sample. Our results, however, indicate that this sample shows weak interaction between Al and H species, marked by the limited dephasing induced by heteronuclear recoupling of these two nuclei. Further, our results indicate that the presence of hydrated aluminum species in the 120-day corroded Ti-5 sample is minor. Therefore, it is likely that another type of structural transformation is taking place in the corroded glass, potentially driven by the dissolution and re-condensation of glass network around Al species that gradually transition into a more ordered state.

The ¹¹B MAS NMR spectra of the corroded glass samples (Fig. 3c) again shows a close overlap with the spectra of the

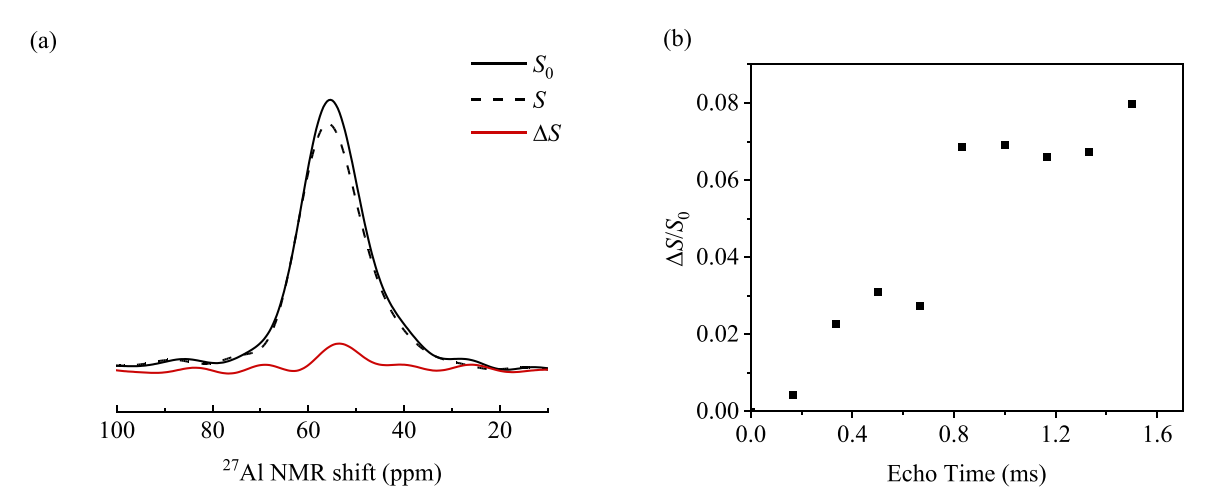


Fig. 4. (a) 27 Al{ 1 H} REDOR NMR spectrum obtained at an echo time of 1.5ms, and (b) 27 Al{ 1 H} effects (Δ S/ 5 0) for the Al(IV) resonance at 56 ppm of the 120-days corroded Ti-5 glass powders. S_0 : spectrum obtained without REDOR pulse; S_0 : spectrum obtained with REDOR pulse; S_0 : spectrum S_0 : spectrum obtained without REDOR pulse; S_0 : spectrum obtained with REDOR pulse; S_0 : spectrum obtained without REDOR pulse; S_0 : spectrum obtained with REDOR pulse; S_0 : spectrum obtained without REDOR pulse; S_0 : spectrum obtained wi

Table 5 Average isotropic chemical shifts (δ^{iso} ; ppm), FWHM (ppm), and calculated fraction (%) of each Qⁿ species in 120-d corroded Ti-5 glass powder, as assessed by ²⁹Si MAS NMR analysis.

Duration	Silicate Species	$\delta^{ m iso}$	FWHM	Calculated Fraction
120	Q^2	-84.4	8.7	14.0
d	$Q^3/Q^2(OH)_2$	-91.5	7.1	12.4
	Q ³ -OH	-100.2	11.9	51.7
	Q^4	-110.4	6.4	21.9
Pristine	$Q^2(2Si)$	-82.5	11.5	9.9
	Q ³ (3Si)/Q ³ (2Si/1Al, B, Ti)	-92.2	13.5	51.5
	Q4(3Si/1Al, B, Ti)	-101.2	10.0	21.5
	Q ⁴ (4Si)	-109.0	15.3	17.1

uncorroded samples. Table 3 lists the calculated N_4 fractions of the post-dissolution samples obtained after deconvoluting their ^{11}B MAS spectra using DMFit. In all the studied compositions except BL and Ti-5, the N_4 fraction decreases slightly after corrosion, but the calculated difference (within \pm 0.8%) lies well within the typical errors assessed while fitting ^{11}B MAS NMR spectra, thus indicating that the borate environment in these glasses remain unaltered (compared to pre-dissolution glasses). On the other hand, the BL, and Ti-5 samples both show a significant decrease in their BO₄ fractions (5.0% and 1.9%, respectively) after 120 days of corrosion in \sim 0.1 M HCl, implying possible preferential release or restructuring of BO₄ units as the corrosion proceeds in these glasses.

To further understand the structural change occurring in the corroded Ti-5 samples, ²⁹Si MAS, ¹H MAS and ¹H \rightarrow ²⁹Si CP-MAS NMR analysis have been performed on both the uncorroded and corroded Ti-5 powders. The obtained spectra are displayed in Figs. 5 and 6. Fitting parameters of the ²⁹Si MAS NMR and the calculated fractions of different structural moieties are listed in Table 5. As shown in Fig. 5, the ²⁹Si MAS NMR spectrum of the as-synthesized Ti-5 glass (Fig. 5a), displaying a broad resonance of tetrahedral Si in the range -75 to -125 ppm, can be fitted with four Gaussian components (centered at -84.4, -91.5, -100.2 and -110.4 ppm, respectively). While each peak represents a potentially distinct silicate species in the glass, a distinct identification of the deconvoluted species is difficult since the chemical shift position is not only affected by its Q^n speciation (where n represents the number of bridging oxygen around tetrahedral Si units), but also by the identity of the next-nearest neighbor species (Si-O-M; where M = Si, Al, B, Ti). Accordingly, glasses containing multiple network-forming oxides can contain several different Si-O-M linkages in the network. For instance, it is well known that the presence of Si-O-Al linkages in alkali aluminosilicate glasses

deshields the ²⁹Si nucleus, thus leading to overlapping peaks between species such as Q^3 and $Q^4(3AI)$ or $Q^3(1AI)$ and $Q^4(4AI)$ [10,99,100]. Additionally, the formation of Si-O-Ti^[5] and Si-O-B^[4] linkages has also been reported to cause downfield shifts in the ²⁹Si resonance [70,101–103] In our case, since all the aforementioned species are present in the Ti-5 glass, the structural complexity of the network is evident. While we are unable to resolve contributions from Q⁴ and Q³ units containing different second neighbors in the spectrum, referring to literature values [10,70,101,104] and ignoring the contribution from Si species that have more than one neighboring Si being substituted by other network formers, we have roughly assigned the four resonances at $\delta^{iso} = -84.4$, -91.5, -100.2 and -110.4 ppm to $Q^{2}(2Si)$, $Q^{3}(3Si \text{ or } 2Si / 1Al, B, \text{ or } Ti)$, Q⁴(3Si / 1 Al, B, or Ti) and Q⁴(4Si), respectively. It can thus be inferred that the as-synthesized Ti-5 glass contains mainly Q³(3Si), Q³(2Si / 1 Al, B, or Ti) and Q⁴(3Si / 1 Al, B, or Ti) species with minor fraction of Q²(2Si) / Q⁴(4Si) units. To supplement this argument with a more quantitative picture of the network connectivity, we have also calculated the NBO fraction in the as-synthesized Ti-5 glass using the tetrahedral Al and B fractions (as determined by NMR), using the expression:

NBO Fraction =
$$\frac{at.\% Na + 2 \times at.\% Ca - at.\% B \text{ in } BO_4 - at.\%Al \text{ in } AlO_4}{at.\% O}$$

In this equation, a few assumptions have been made, for instance, we assumed that: (1) Ti^{4+} incorporates in the network as TiO_4 due to its low concentration, and therefore, will not affect the connectivity of the silicate network [70,105], and (ii) Na^+ and Ca^{2+} are first consumed by BO_4^- and AIO_4^- units as charge compensator; the excess modifier charge then creates NBOs in the silicate network on a 1-for-1 or 1-for-2 basis, respectively [73]. The calculated NBO fraction is \sim 13.7%, corresponding to an average Si

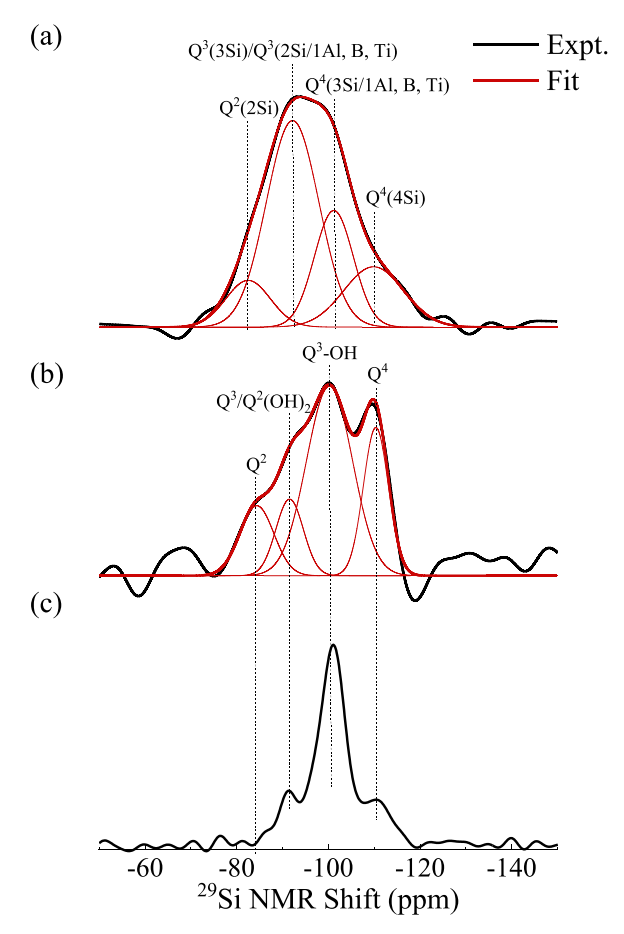


Fig. 5. ²⁹Si MAS NMR spectra of the (a) un-corroded and (b) 120-day corroded Ti-5 glass; (c) $^{1}\text{H}\rightarrow^{29}\text{Si}$ CP-MAS NMR spectra of the 120-day corroded Ti-5 glass. The ^{29}Si MAS NMR spectrum was fitted with four Gaussian/Lorentz functions (red line) corresponding to the Qⁿ resonances; the position of each component is indicated by the black dash line.

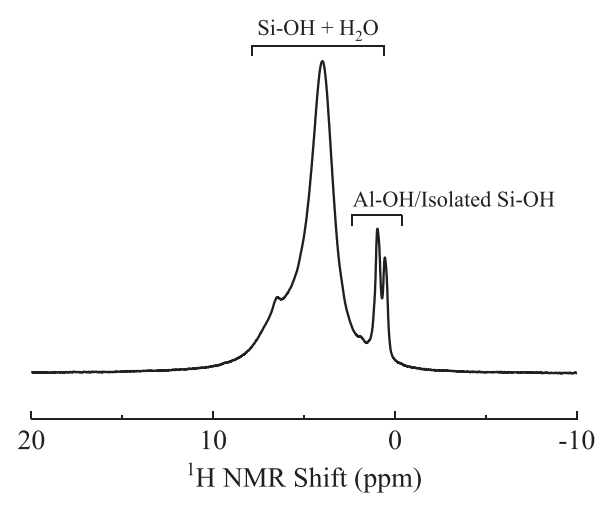


Fig. 6. ¹H MAS NMR spectrum of the 120-day corroded Ti-5 glass.

connectivity of 3.49, which is in satisfactory agreement with the fitted Si speciation from the 29 Si NMR spectrum (fitted Si connectivity: 3.29). Therefore, on an average, roughly half of the Si species are Q^3 , and half are Q^4 , where each may contain distinct nextnearest neighbor species.

As compared to the as-synthesized glass, the ²⁹Si MAS NMR spectra of the 120-day corroded Ti-5 sample (Fig. 5b) starts to

show more resolved features, highlighting the effect of acid corrosion on the glass structure. Deconvolution of the spectrum clearly demonstrates the contribution from four distinct environments, with resonance peaks centered at -83.9, -91.7, -100.0 and -109.5 ppm. The latter three peaks noticeably align closely with the three peaks displayed in the CP-MAS NMR spectrum (Fig. 5c). Therefore, in accordance with the literature [10,103,106], we have attributed the -100.0 and -109.5 ppm peak to Q3-OH and Q4 species, respectively. The Q³-OH is expected to stem from the hydrated silica (i.e., Si-OH, as also indicated by the FTIR result) in the altered layer, either resulting from ion exchange at NBO sites or hydrolysis, and thus shows strong interaction with hydrogen in the CP-MAS spectrum. The Q4 signals likely arise as a result of cross-polarization to protons at greater ¹H-²⁹Si internuclear distances. The assignment of the peak centered at -91.7 ppm, however, is more challenging as it may be correlated to Q²(OH)₂, which has been previously suggested by Angeli et al. [10] or coming from non-silanol Q³ species in the sample, as Q3 units in silicate and borosilicate glass are generally reported around this position [104,107,108]. With the current data, we are unable to determine the exact origin of this peak. However, the resonance peak centered at -83.9 ppm, which is not evident from CP-MAS NMR spectra, most likely originates from the bulk, pristine (unaltered) portion of the glass. Also, due to the above-discussed uncertainty in peak assignments, the effect of varying second nearest neighbors is not considered here. This fitting gives an average calculated Si connectivity of 3.02 (assuming a similar distribution of Q^3 and $Q^2(OH)_2$ species for an average connectivity of 2.5), displaying that acid corrosion has induced a serious breakdown of the Si network by hydrolysis.

The ¹H MAS NMR spectrum of the post-dissolution Ti-5 sample (Fig. 6) can be roughly resolved into four components: (i) Two broad peaks at 4 and 6 ppm, corresponding to molecular water and hydrogen-bonded silanol groups in the alteration layer [10,109–111] and (ii) two overlapping narrow peaks at 0.5 and 1 ppm, which may be attributed to Al-OH or isolated silanols in which the proton is not bound to another oxygen through hydrogen bonding [10,112]. Combining these results, the formation of a silica gel layer on the corroded Ti-5 glass can thus be inferred. Though we are unable to calculate the detailed Si speciation in the glass due the compositional complexity, the significant increase of Q⁴ fraction (+4.8%) in the corroded sample emphasizes the possibility of network recondensation within the hydrated silica layer during corrosion, which is in good agreement with the mechanism previously proposed for borosilicate glass leached in acidic environment [10,20,113].

3.3.3. Surface chemistry of corroded glasses

While the MAS NMR spectroscopy helps us understand the evolution in the bulk structure of glasses because of aqueous corrosion, XPS has been employed to understand the chemical transformations occurring near the glass-solution interface. Fig. 7 presents a comparison of the core level XPS spectra of all constituent elements in the polished glass coupons before and after corrosion in 0.1M HCl for 120 days. The concentration of Na, Ca and Al in the \sim 5-10 nm deep (probe depth of XPS) surface of corroded glass is below the detection limit of XPS, as emphasized from the absence of peaks in the core level spectra for each element (Fig. 7a-c). It should be noted that the broad peak (~347 eV) observed within the Ca 2p window of the corroded Zr-5 sample (Fig. 7b) is indeed associated with a shifted Zr 3p1 peak (instead of Ca 2p) due to remaining Zr species at the surface. This result is further proven by the absence of Ca 2s peak in the survey spectrum of the same sample (Fig. S7). Similar to Na, Ca, and Al core-level spectra, the intensities of B 1s peaks are also significantly reduced in the corroded samples (Fig. 7d). Here the peak with an asterisk centered at \sim 196 eV in the pre-dissolution glass La-5 should be attributed to

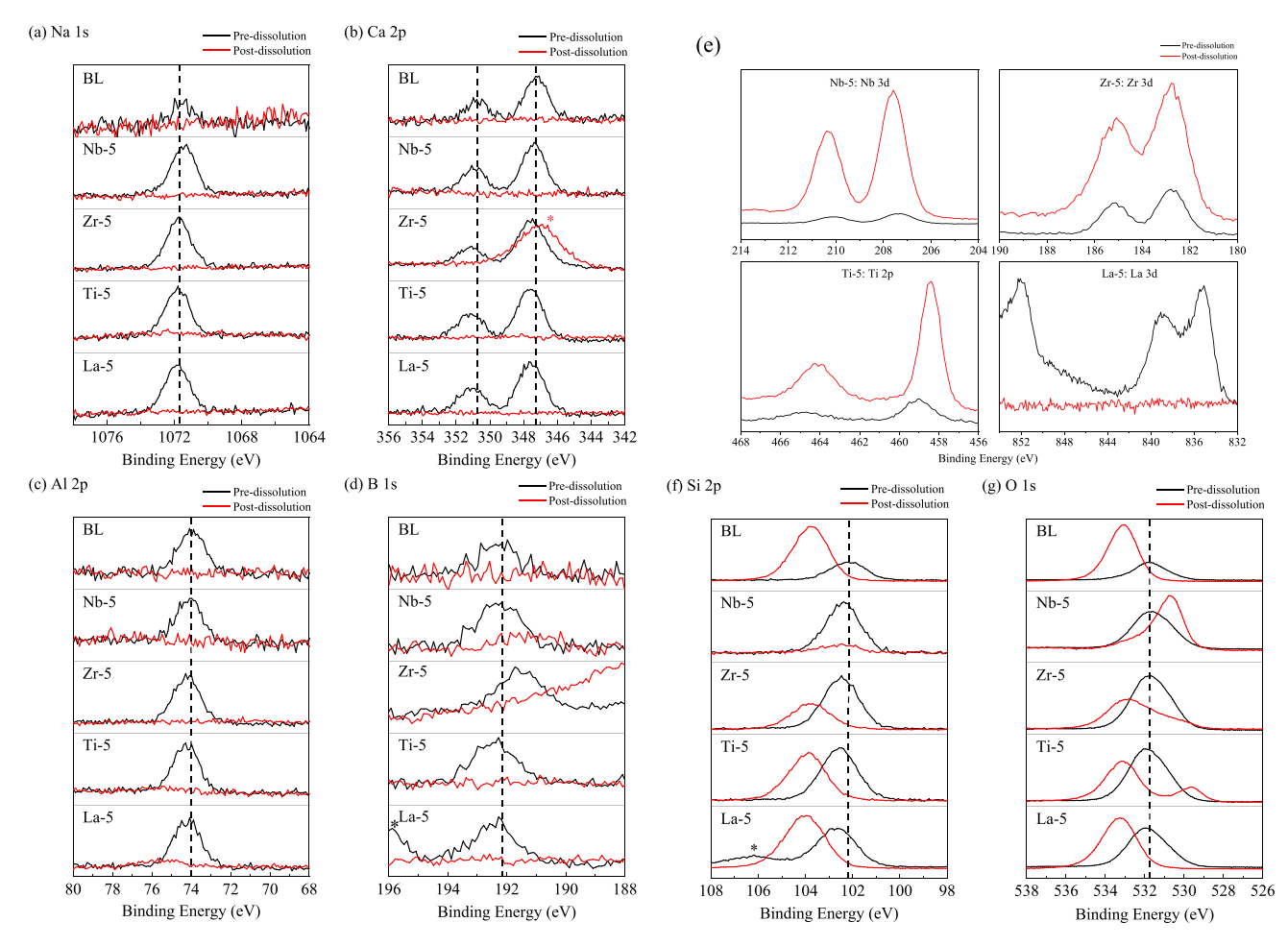


Fig. 7. (a) Na 1s, (b) Ca 2p, (c) Al 2p, (d) B 1s, (e) Nb 3d, Zr 3d, Ti 2p and La 3d, (f) Si 2p and (g) O 1s XPS spectra of the polished (un-corroded) and 120-day corroded glass samples. The * in Ca 2p, B 1s and Si 2p core-level spectra indicate signal from shifted Zr 3p, La 4p and La 4d photoelectrons, respectively.

Table 6 Elemental composition (atom %) of polished and corroded glass coupons as measured in the top \sim 5-10 nm surface via XPS analysis (atomic percentages accurate within \pm 5%).

Sample	ID	Na	В	Si	0	Al	Ca	Nb	Zr	Ti	La
BL	Polished	8.0	3.3	14.6	68.9	4.3	0.9	_	-	-	_
	120 d	0	0.6	23.9	75.5	0	0	-	-	-	-
Nb-5	Polished	7.9	4.6	12.3	68.4	3.1	1.8	1.8	-	-	-
	120 d	0	1.7	2.4	76.5	0	0	19.4	-	-	-
Zr-5	Polished	6.3	4.7	14.3	67.9	3.8	1.7	-	1.3	-	-
	120 d	0	-	13.3	78.8	0	0	-	7.9	-	-
Ti-5	Polished	5.8	4.8	14.8	68.3	3.7	1.2	-	-	1.4	-
	120 d	0	1.3	17.1	72.9	0	0	-	-	8.6	-
La-5	Polished	5.3	4.1	17.8	66.7	3.7	1.1	-	-	-	1.3
	120 d	0	0	24.1	75.2	0.8	0	-	-	-	0

La4p signal. Also, in the 120-day Zr-5 sample, B 1s signal is masked by the tail of the nearby Zr 3d doublet peak and thus cannot be assigned. Since the quantification of the XPS results is subject to the influence of peak interference, and the detection limit of the instrument can vary significantly with the cross section of the core state of interest and the background signal level (i.e., matrix effect), STEM adjoined with EELS has also been employed on the post-dissolution samples as a complementary technique to get a more precise understanding of the surface elemental compositions, which will be discussed later in this section.

The surface compositions of the pre- and post-dissolution samples are estimated based on fitting of the core level spectra and the results are listed in Table 6. As indicated by the calculated values, while a significant enrichment (\sim 6 to 10 \times , as compared to

pre-dissolution samples) of network reticulating HFSCs, i.e., $\mathrm{Nb^{5+}}$, $\mathrm{Zr^{4+}}$ and $\mathrm{Ti^{4+}}$, is observed in the altered surface of the Nb-5, Zr-5 and Ti-5 samples, respectively, the La content in the corroded La-5 glass is below detection limit of XPS (Fig. 7e). This is in agreement with the NL data of La-5 sample showing the congruent release of La (along with Na, Ca and B in the residual rate regime) from the glass into the solution. A relatively smaller but substantial increase in the Si concentration (\sim 1.2 \times to 1.6 \times) can be observed on the surface of all post-dissolution samples except Nb-5 and Zr-5 when compared with the pre-dissolution samples (Fig. 7f). The Nb-5 and Zr-5 compositions, on the other hand, exhibit depletion (but not full exhaustion) of the surface concentrations of Si. It should be noted that XPS is only looking at the top few nanometers of the sample surface, therefore, the minor retainment (or incorporation)

of Si in the Nb-/Zr-rich altered layer, as indicated by the XPS result, may not be reflected in the ICP-OES measurement (which is usually in the ppm range). As a result, for these two glasses, the NL plots from the ICP-OES data show a congruent dissolution pattern between Si, Na, Ca and Al. Nonetheless, this result indicates that in the Nb-5 and Zr-5 glass, significant formation of silica gel layer has not yet started. Moreover, it is observed that the Si 2p peak shifts towards higher energy (~0.2-1.6 eV) upon corrosion in all the studied glasses, reflecting a general decrease in the electron charge density around the surface Si atoms. Such a modification may be attributed to the change in the surface composition and structure of the sample, as the polished, uncorroded glass surface transitions towards a hydrated altered layer that is dominated by re-precipitated Si- or HFSC-containing product(s) [114,115].

In terms of oxygen speciation, the asymmetric nature of the O 1s peaks observed for both the uncorroded and corroded samples (Fig. 7g) suggests the presence of several underlying peaks associated with different local binding environments of oxygen in the sample surfaces, e.g., bridging oxygens (BOs) (~532.5 eV) and NBOs (531.0 eV) in the silicate glass network [116-118]. The shift towards higher binding energy upon corrosion as observed in the O 1s (and also Si 2p) spectra of all the samples but Nb-5 (which is highly depleted in Si) is in agreement with the literature on borosilicate glasses and silica gel layers [119,120]. Interestingly, a secondary peak centered at \sim 529.5 eV appears in the O 1s spectrum of the post-dissolution Ti-5 sample, which may be attributed to formation of Ti-rich dissolution product (previously reported values for TiO2-O range from 529.5 to 530.6 eV) [121-123]. Such change is also observed for the 120-day Zr-5 samples, in which a shoulder centered at ~530 eV can be seen upon corrosion (reported O 1s binding energy ranges from 529.6 to 531.2 eV for ZrO_2) [124–127]. This irregularity in the O 1s peak shape likely highlights the impact of the formation of Ti/Zr-containing crystalline/amorphous secondary

product(s) (as also indicated in the NL data) on the surface structure of these samples, and it can be inferred that the enrichment of this secondary product (with respect to the silica gel layer) on the surface is much more significant in the Ti-5 sample than Zr-5 sample owing to the faster dissolution kinetics of the former. Similarly, for the Nb-5 glass, the appearance of a symmetric O 1s peak located around 530.7 eV upon corrosion should be related to the formation of Nb/O-containing corrosion product (reported Nb₂O₅-O 1s binding energy: 529.6 to 531.3 eV) [128-131], consistent with the results of ICP-OES and Nb 3d XPS data, which suggests the precipitation of Nb on the glass surface after corrosion. However, due to the co-existence of various oxygen species with similar binding energies, precise O 1s peak assignment for multicomponent oxide glasses may sometimes be difficult or even infeasible. Therefore, the analysis of the O 1s spectra has been limited to quantification of the total oxygen content on the sample surfaces before and after corrosion. As shown in Table 6, a 5-11% increase in the oxygen content can be estimated on the surface of glasses (irrespective of composition) as a result of glass-acid interactions.

As mentioned earlier, STEM and EELS have been employed on the 120-day corroded glass powders to complement the XPS results. The high angle annular dark-field (HAADF) images taken near the surface of the corroded glass particles of each composition with corresponding EDS maps are shown in Fig. S8-S12. For all the studied samples, layers of different chemical makeup can be observed within the corroded powders, confirming the formation of alteration layer(s) that are chemically different from the predissolution glass powders. While the crystalline phase has been identified in the Ti-5 sample by XRD, it is not detected during the TEM analysis, possibly due to the smaller sample size. However, its HAADF image clearly depicts a Ti-enriched area near the surface (Area #3 – Fig. S11). Additionally, minor concentrations of boron have been detected in the altered layer of all the glass powders,

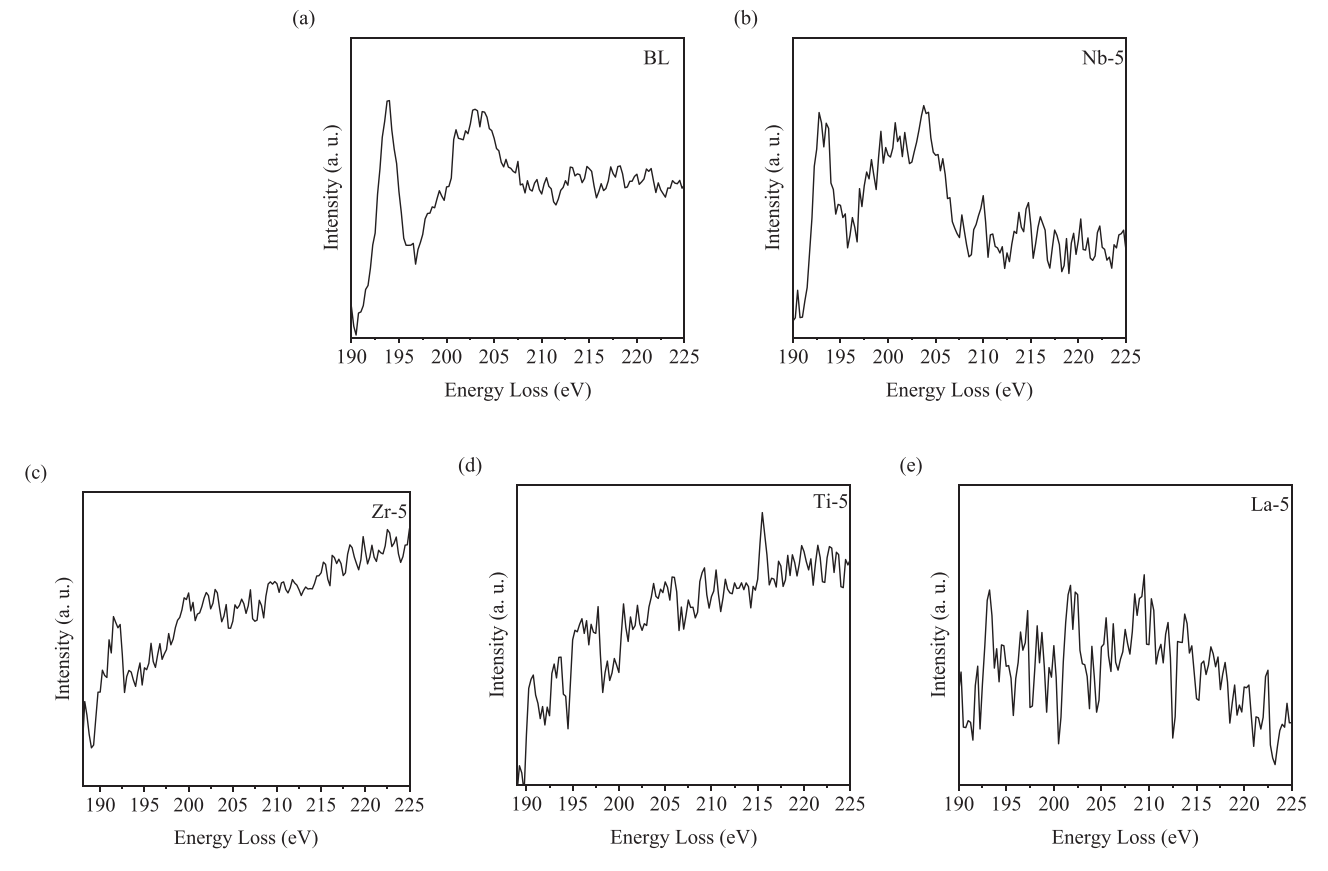


Fig. 8. EELS spectrum from the surface region of post-dissolution (a) BL, (b) Nb-5, (c) Zr-5, (d) Nb-5 and (e) La-5 glass powders showing the boron K-edge near 190 eV.

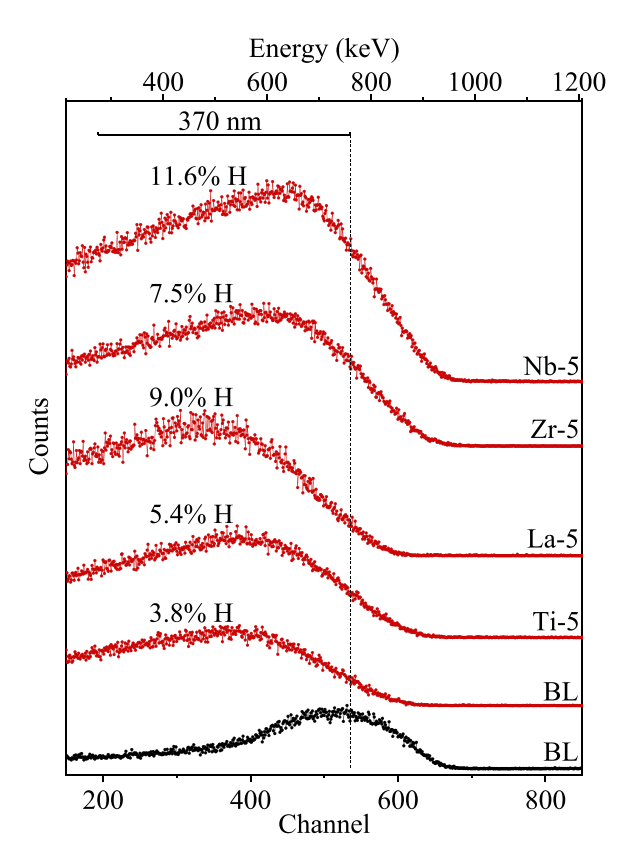


Fig. 9. ERDA-measured hydrogen profiles of the 120-day corroded glass coupons (red line) and the polished (un-corroded) BL glass coupon (black line). The hydrogen concentrations displayed have been estimated for the top 370 nm of the samples.

as evident from the B K-edge at \sim 190 eV in the EELS spectra obtained near the surface of the corroded samples (Fig. 8). This result suggests that for the studied glass compositions, some boron stays in the alteration layer resulting either from incomplete dissolution of the B network or from reprecipitation of dissolved B species during corrosion processes. Similar results discussing the possibility of boron incorporation in the alteration layer during the dissolution of borosilicate glasses have been reported in the literature [62,132]. In the present study, considering the faster boron release during the forward rate regime followed by its slow down, it is likely that boron precipitates back on to the glass surface and is retained in the altered layer during the dissolution.

To gain further insights into the formation and reconstruction of the hydrated altered layer during aqueous corrosion, ERDA has been performed on the 120-day corroded samples and the results showing the hydrogen incorporation in the top 370 nm of the sample surface are presented in Fig. 9. The surface of glass is indicated by the vertical black dotted line in the figure and the energy of the detected recoiled particles can be converted from their channel scale through a factor of 1.42 keV per channel. As shown in the spectrum, the channel at which the maximum count of hydrogen signals is measured follows the order: Nb-5>Zr-5>Ti-5≈BL-5>La-5 glass. While this scale can be affected by factors such as surface charging or energy loss due to collision with the substrates, generally this scale is negatively correlated to the depth of the detected species in the sample, i.e., peaks with higher channel/energy refer to species that are closer to the surface. Therefore, it can be inferred that the altered layer of the corroded Nb-5 and Zr-5 sample seems to be dominated by hydrogen species that are closer to the surface, whereas the other samples are dominated by hydrogen residing deeper into the surface.

Further, using the pre-dissolution glass samples as reference (which typically contains <0.1% H, as shown in our previous study [19]), the surface hydrogen contents are calculated as 3.8, 5.4, 7.5, 9.0 and 11.6 atom% for the 120-day BL, Ti-5, Zr-5, La-5, and Nb-5 samples, respectively. Such a significant increase in the surface hydrogen content clearly indicates the formation of hydrated alteration layer(s) on the surface of the corroded glasses, in agreement with the ICP-OES and XPS results demonstrating incongruent dissolution in all the investigated compositions.

The differences in the concentration and depth of hydrogen content in surface of the corroded glasses may be related to several factors including the (i) degree of corrosion, (ii) type and amount of resultant hydration products, and (iii) chemistry and structure of the alteration layer. Therefore, the ERDA results need to be inferred in combination with the results from the other spectroscopic characterization techniques, i.e., ICP-OES, XPS. In the present study, while the glasses BL, Ti-5 and La-5 exhibit higher NL values after 120-day corrosion compared to the glasses Nb-5 and Zr-5, the plateau in the NL curves of the former (BL, Ti-5 and La-5) indicate their dissolution has already been passivated due to the formation of Si-OH gel layer on their surfaces. As revealed in the literatures, the structure of the SiO₂-rich alteration layer can continue to evolve through recondensation after its formation; such structural reorganization towards densification and pore closure plays a crucial part in passivating the dissolution as it limits the transport of aqueous species to the pristine glass surface [7,31,133-136]. Therefore, the effective passivation observed in the glasses BL-5, Ti-5, and La-5 suggest that their surface silica gel layer has already undergone reorganization and densification. We believe this maturation process of the gel layer can cause lower H content near the surface due to the more condensed surface structure, as reprecipitation, and thus condensation, occurs fastest near the reacting front; It has also been shown that during the reorganization process, water can still diffuse into the Si gel layer and being trapped in closed pores, leading to the observed H retention deeper into the surface [132,135,137]. As compared to the corroded BL glass, the higher hydrogen content measured in the 120-day Ti-5 sample can be attributed to the presence of Ti-bearing hydrated precipitate along with Si - OH layers. Further, the higher H content on the surface of corroded La-5 sample may be attributed to its faster dissolution kinetics resulting in the formation of a thicker and mature silica gel layer. Here it needs to be emphasized that the ERDA only measures the top 370 nm of the sample surface. Therefore, the presence of hydrogen species deeper in the surface layer may not be readily detected. Thus, the calculated hydrogen content from the ERDA may not represent the entire hydrated layer.

On the contrary, the NL profiles and the surface chemistry (by XPS) of the corroded Nb-5 and Zr-5 samples suggest that the dissolution in these glasses has not reached the residual rate regime by the end of the 120-day experiment. Thus, the formation/precipitation of Si-OH layers on the surface of these glasses has either not initiated or their concentration is below the detection limit of the characterization techniques used in the study. Instead, the surface of these two samples is covered by loosely bound layer(s) of Nb (in Nb-5) and Zr (in Zr-5) based dissolution products. It is likely that these layers have adsorbed/absorbed water resulting in high H content and distinct hydrogen profiles as compared to that of the corroded BL, La-5 and Ti-5 glass.

4. Discussion

4.1. Insights into the mechanism of glass dissolution in acidic conditions

The literature on the topic of glass corrosion in acidic media reveals only a handful of studies focused on understanding the

mechanism and kinetics of dissolution in a narrow set of glass chemistries, with most of them being vitrified analogs of SiO₂-rich natural minerals [16–18,21,138–144], a few being simplified borosilicate-based nuclear waste glasses [20,145], and others being on aluminosilicate-based E-glass [146,147]. Consequently, there is a lack of consensus in the literature on the fundamental mechanisms governing the dissolution of multicomponent silicate glasses in acidic solutions that applies to a wide composition space.

The literature on this subject debate two basic mechanisms for silicate glass corrosion: (i) the classical multi-step interdiffusion-based mechanism and (ii) the interfacial dissolution re-precipitation mechanism (IDPM) [20]. The former describes the mechanism of corrosion as a multi-step process that includes release of mobile glass modifying cations (such as Na+) through ion exchange with protons in solution to form hydrated Si-OH bonds (forming an inter-diffusion layer), followed by the protonation and hydrolysis of bridging bonds (i.e., Si-O-Si or Si-O-Al) and restructuring of the hydrated silica network into a gel layer via repolymerization reactions [148–151]. The IDPM, on the other hand, suggests that glass corrosion proceeds as an inward-moving reaction front in which all bonds at the glass-fluid interface break and are immediately re-precipitated to form an amorphous gel layer [20]. The supersaturated water at the interface not only promotes alkali/alkaline-earth release from the glass but in fact releases all elements in the outermost surface layer only to reorganize as a secondary phase of network forming species such as Si and Al [20]. While the classical inter-diffusion-based mechanism has been widely accepted in the glass community, recent studies suggest that a basic mechanism describing silicate glass corrosion may be more complicated than assumed in either individual mechanism, with high dependence upon glass composition and surrounding leaching conditions [150,152,153]. The most recent literature on this topic suggests the above discussed mechanisms of glass corrosion are not necessarily mutually exclusive, as transition from IDPM to partial hydrolysis-in situ reorganization has been observed in one single experiment, following the formation of a continuous precipitated layer [135]. However, that experiment has been performed at pH = 9, and therefore may be distinctly different from

In the preface to the discussion about the mechanism of glass dissolution in the present study, it needs to be highlighted that the incorporation of HFSCs into the glass structure, and their reprecipitation during the dissolution, does not alter the reaction mechanism in the investigated glass system. The impact of HFSCs on the kinetics of dissolution of the investigated glasses will be discussed in the next section.

In the present investigation, we clearly detect a slower release of Si from the BL, Ti-5 and La-5 glasses starting from their rate drop regions followed by a significant retention of Si in the alteration layer. Nonetheless, these results alone do not unambiguously support one mechanism of glass dissolution over the other. However, when these results are viewed in combination with the slow but congruent dissolution of glasses Nb-5 and Zr-5, the dissolution of these glasses seem to follow the IDPM model, wherein, at the early stages of the experiment, the glasses dissolve congruently due to the strong proton attack at pH = 2, thus, hydrolyzing the various linkages in the glass indiscriminately despite their intrinsically different bond energies. The fast release of constituent elements then quickly leads to local supersaturation, and therefore, re-precipitation of less soluble species, e.g., silicates, at the glass surface, thus, forming amorphous Si-rich gel layer that recondenses and passivates the reaction.

As the experiments proceed to 120 days, while the slow (and congruent) release of Nb-5 and Zr-5 glasses still exhibit a dissolution pattern that can be well defined by IDPM, the structural characteristics of heavily corroded BL, La-5, and Ti-5 glass powders de-

viate from what would otherwise be expected from a purely IDPM-controlled glass dissolution. Specifically, the ²⁷Al MAS and ²⁷Al{¹H} REDOR NMR spectra of Ti-5 glass (Fig. 4) reveals that upon corrosion, this glass undergoes a structural transformation towards a more ordered network around Al, and such process is seemingly not related to the precipitation of hydrated Al species. For instance, it has been observed by CP-NMR that the Al-H interaction in this glass is minor—thus, the amount of hydrated Al is too insignificant to cause the observed narrowing of the ²⁷Al resonance. Therefore, another process must be taking place in conjunction with the IDPM during the corrosion.

As demonstrated in the literature [132,154,155], glasses dissolved through IDPM usually form an ultrathin interfacial solution layer between the pristine glass and the outer alteration layer, which is thus considered as characteristic of IDPM. The reaction front described for glasses undergoing IDPM is relatively sharp, leading to abrupt changes in structure and chemistry when comparing the uncorroded glass surface with the hydrated layer. However, the interfacial solution in this region can exhibit a pH and concentration gradient. Additionally, ion transport and water diffusion does not necessarily cease within the amorphous Si-rich layer [135,144,150]. It can thus be inferred that ion exchange/network hydrolysis can still occur on the pristine glass surface even after the formation of an alteration layer, but the kinetics may not necessarily be the same. Consequently, two possible scenarios may contribute to the observed structural rearrangement around Al, as discussed below.

- (1) The formation of a highly concentrated interfacial solution near the uncorroded glass surface, as well as the reorganization of Si gel layer, imposes a kinetic barrier for protons migrating towards the glass, thus, weakening the acid attack on the glass network. As a result, congruent dissolution can no longer be maintained, but instead preferential leaching of less tightly bound species and *in-situ* reorganization of the residual network takes place. Since Si-O-B and B-O-B linkages are more readily hydrolyzed than Si-O-Si and Si-O-Al linkages [19,156], one can thus imagine a more condensed/polymerized and less distorted network around Al forming as a result of the recondensation process near the reactive interface.
- (2) Alternatively, Al, and other constituent components, still leach out congruently from the glass surface, but they interact with the alteration layer and are being trapped in it before they can reach the bulk solution, i.e., they are not measurable by the ICP-OES, thus accounting for the reduction in rate of elemental release with time, as observed in the NL plots, Additionally, Lenting et al. [152] reported a dense interfacial layer enriched in Si between the outer alteration layer and the pristine glass (at pH = 7-8), which they attributed to the precipitation and condensation of dissolved Si species from the interfacial solution during the rinsing and drying procedure of the glasses after the conclusion of dissolution experiments. Although the experimental conditions in the present study are significantly different from those discussed by Lenting et al. [152], the glasses in each study have gone through the same mechanism of dissolution, i.e., IDPM, including similar rinsing and drying procedures (after the conclusion of experiments). Therefore, it is likely that the observed structural changes around Al, in the present study, are caused by local reorganization of Al in the alteration layer during the experiment, and/or similar precipitation and recondensation processes at the interface between the glass and the alteration layer during the post-dissolution treatment, as discussed by Lenting et al. [152].

In summary, both scenarios may lead to unexpected structural evolution in glasses, as observed in BL, Ti-5 and La-5 glasses. While the current dataset cannot distinctly distinguish one scenario from

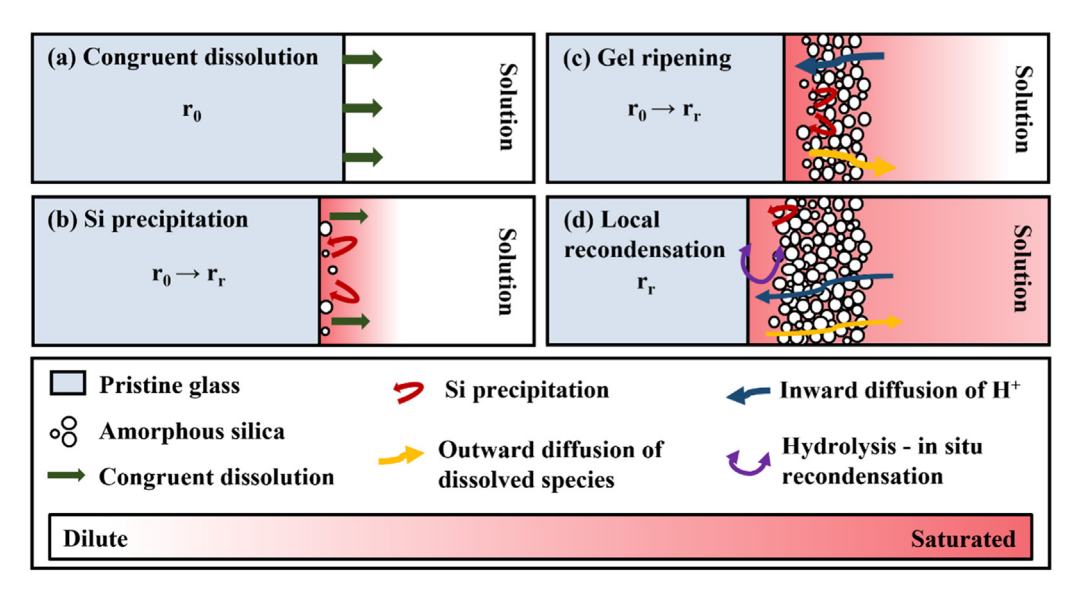


Fig. 10. Graphical representation of the IDPM/in-situ recondensation coupled model. (a) At pH = 2, glass dissolution starts with congruent release of all constituent elements at forward rate r_0 . (b) The fast initial dissolution leads to Si supersaturation and hence precipitation near the glass surface, initiating the transition towards residual rate (r_r) behavior. (c) The structure of the amorphous Si–OH layer evolves towards densification upon its formation; In the meantime, ion exchange/network hydrolysis continues at the reacting front. (d) The transportation barrier (of protons and dissolved glass species) imposed by the densified Si–OH layer is eventually strong enough to initiate *in-situ* recondensation near the interfacial solution between the pristine glass surface and the amorphous silica layer.

the other, it is clear that at pH = 2, the dissolution of the studied aluminoborosilicate glasses is not exclusively governed by IDPM, but instead better depicted by an IDPM/*in-situ* recondensation coupled model, wherein IDPM leads to the formation of Si-rich alteration layer at the early stage of dissolution, local recondensation then takes place within the altered zone due to limited kinetics. A graphical representation of the proposed model is shown in Fig. 10.

Finally, while boron is generally considered as not being retained in alteration layer under acidic pH [20,145,157], our results suggest it is not necessarily the case, as TEM-EELS analysis depicts the presence of boron in the altered region of the corroded glass particles, either through re-precipitation or retention. This observation is consistent with our previous results showing slower release of B compared to Na, Al and Si during the residual rate regime of a series of sodium aluminoborosilicate glasses leaching at pH = 2 [19]. We thus suggest that the possibility of B incorporation in the alteration layer cannot be neglected under acidic condition, and the common practice of using B as the tracer element for modelling dissolution progress may need re-evaluation.

4.2. Compositional and structural dependence of dissolution kinetics in the investigated glass system

Comparing the results of the HFSC-containing glasses to that of the BL glass, the effect of incorporating HFSCs into the borosilicate glass system on the dissolution behavior of the resultant glass at pH=2 is revealed, and this effect must be understood in the context of the structural changes induced by the HFSC species in each glass.

Upon exposure to acidic pH, substituting BL composition with La³⁺ leads to an extensive acceleration of the glass dissolution kinetics. This result may be explained by the hypothesis that the La-5 glass seemingly exhibits nanoscale phase separation (deduced from the DSC curve and from previous literature[44]), and that the La-rich alkali borate phase is likely more soluble in acid in comparison to the homogeneous glass network of BL glass. However, La-5 glass also exhibits faster and more efficient passivation (marked by the stable NL value) than that of the BL glass, which should be attributed to a more mature Si gel layer. Therefore, it seems faster dissolution kinetics can lead to faster formation and reorganization

of the amorphous silica layer. In contrast, for BL glass, the slower release kinetics leads to slower and less complete recondensation of the alteration layer, therefore, BL glass shows progressively more release in the residual rate regime as compared to the La-5 glass. However, if the corrosion is allowed to proceed for prolonged durations, i.e., beyond 120 days, it is also possible that the alteration layer of BL glass may eventually densify and change the corrosion behavior to resemble that of the La-5 glass.

On the other hand, the presence of network reticulating HFSCs, i.e., Nb⁵⁺, Zr⁴⁺ and Ti⁴⁺, impacts not only the reaction kinetics but also the dissolution pattern as well as the chemical makeup of the alteration surface at pH = 2. For example, the incorporation of Nb⁵⁺ and Zr⁴⁺ lead to much slower congruent initial dissolution behavior while the Ti-5 glass behaves similar to the BL glass, dissolving incongruently due to the slower release of Si. It is also observed that the corroded Ti-5 glass surface is enriched in Si, while the altered surfaces of Nb-5 and Zr-5 glasses are depleted in Si and enriched in Nb/Zr, respectively. Combining all the results, we believe these differences occur because of the vast disparities in corrosion kinetics, and hence the reaction progress during the experiment, but not necessarily the reaction mechanism. Specifically, Nb⁵⁺ participates in the network as NbO₆⁻ units with intense Nb-O interactions, [56,57] which strengthens the glass network so much that the network hydrolysis in this glass is extremely retarded, and that an obvious Si saturation cannot be observed throughout the length of experiments. Accordingly, the altered surface is instead encompassed by precipitated Nb species, as opposed to Si in a gel layer. Similarly, the incorporation of Zr⁴⁺ in the glass also slows down the network hydrolysis, but not as significantly as for Nb⁵⁺ as Zr⁴⁺ is less charged. It can be observed that the NL plot of Zr-5 sample displays a gradual deviation of Si release from congruency after 60 days, at which point the NL value of Si is $\sim 75~\text{g/m}^2$, comparable to the onset value of Si plateau observed for the BL, La-5 and Ti-5 glass (~69, 87, 78 g/m², respectively). Therefore, it is also possible that this glass has entered an early stage of Si saturation in which an Si-containing (13.3 vs. 14.3 atom% for the uncorroded surface) alteration layer is able to form but has not yet densified. In contrast, the addition of Ti⁴⁺ does not strengthen the glass network as effectively as Zr⁴⁺ and Nb⁵⁺ does, as it is generally present in the network in TiO₄ and TiO₅⁻ form

when present in low content [70,105]. Therefore, the dissolution kinetics of the Ti-5 glass, although slightly slower, still facilitate a rapid Si saturation, hence allowing the formation and ripening of a Si-rich passivating layer and rapid Ti phase precipitation. Notably, we observe that the onset of Ti precipitation, as indicated by the drop in the Ti NL curve, does not coincide with that of the Si NL curve. Moreover, inhomogeneous distribution of Ti/Si with area showing particular Ti enrichment (but not Si) was observed in TEM. These observations, along with the results from other glasses, likely suggest that formation of an amorphous silica layer is independent of the precipitation of Ti, Zr, or Nb, but rather controlled by local Si saturation near the glass-water interface, as has also been proposed by Geisler et. al. [20] However, this result does not fully exclude the potential long-term effect of a re-precipitated HFSC layer on the dissolution kinetics since, particularly for the Zr-5 and Nb-5 samples: (i) the experiments only lasted for 120 days with slow release kinetics, leading to a slow transition into stage II, and (ii) the HFSC-enriched layers are likely only a few nanometers thick after 120 days (as seen in SEM, data not presented). Due to these limitations in the current data and the competing effects of silica gel layers forming on the glass surface (as in the case of Ti-5), it is difficult to comment on the distinct effect of HFSC-rich layers on the release kinetics. Nevertheless, it is possible that with more time and surface-layer maturation, a particular long-term effect of HFSC species can be unearthed, which to our knowledge, has not been reported in the literature. Thus, further examination of long-term behavior and the resulting surface layers is required.

4.3. Technological implications of the results

The aluminoborosilicate glass family forms the basis for a wide range of advanced industrial glasses [158–162], and the acidic corrosion behavior of these glasses is critical for their practical application. Whether it is reducing the thickness of glass substrates for flat panel displays [163,164] or lessening the severity of surface flaws on chemically strengthened cover glasses [159], or designing ultra-thin glasses for photonics [165], acid etching technology has enabled several such ideas to develop from concept to reality [166]. Therefore, it is of utmost importance to understand and establish the compositional and structural dependence of acid etching in the glasses from alkali/alkaline-earth aluminoborosilicate family.

As discussed earlier, the literature on this subject approaches the problem from an academic viewpoint with minimal tangible implications on improving or optimizing the process of acid etching in the glass industry. For example, the etch rate of a glass is the most important consideration for economic implementation of the acid-thinning approach, since a longer etch time leads to lower throughput (and higher cost) on the production line. Therefore, it is vitally important to understand the relationship between glass composition and etch rate in a highly acidic environment, as this information can be used to guide the development of the next generation of display substrate materials. However, the lack of a rigorous scientific understanding regarding the corrosion behavior of multicomponent and compositionally complex glasses has forced industrial processes to be developed based primarily on empirical data.

In the abovementioned context, the results discussed in the present study have significant scientific and technological relevance. While the scientific relevance pertaining to the new insights into the mechanisms of glass corrosion in acidic solutions and revealing the structural drivers controlling the kinetics of glass dissolution have been discussed in the previous sections, the technological relevance of the work can be gauged from the fact that the high ionic field strength cations are an integral part of many industrial glasses. As an example, nearly all industrial glass-melting is performed in melting tanks built from ZrO₂-containing refrac-

tory bricks [167]. In many cases, the refractory bricks are pure ZrO₂. In other cases, AZS (alumina-zirconia-silica) refractories are used. Therefore, even if ZrO₂ is not specifically incorporated into the batch materials, the final glass product always contains some non-zero concentration of ZrO2 due to dissolution of the refractory bricks during the glass melting process [168]. Further, higher temperature melting, and longer residence times generally lead to a greater concentration of ZrO2 being incorporated into the final glass product. The presence of undesired amounts of ZrO2 in the final glass product can have serious economic implications as ZrO₂ tends to considerably slow down the kinetics of glass corrosion in the acidic solutions, as shown in the present study. This will result in lower rate of etching of the glass, thus leading to a lower throughput (and higher cost) during production. The problem of slower etching rate in acids gets further exacerbated in glasses containing Nb₂O₅, an important component of glass-ceramics with unique dielectric properties with applications in microelectronics [169].

Another problem highlighted from the results of the present study is that of the behavior of chemical etching of glasses, i.e., congruent vs. incongruent release. While most functional glasses are expected to undergo uniform isochemical etching [158], all the high field strength cations (except La³⁺) in the present study tend to precipitate on the surface of glass, even during the early stage of reaction. This is undesirable from the viewpoint of achieving an isochemical etch as the precipitated products can act as a passivating layer, thus, hindering the process of etching. Even worse, the enrichment of HFSCs on the surface may change the surface properties of the materials, thus harming its performance.

Therefore, although it is imperative to work towards understanding the compositional dependence of chemical etching in multicomponent silicate glasses over a broad compositional space, it is also equally important to work towards designing solutions that can give uniform isochemical etches of a given glass composition. Finally, the results presented in the article feed into the bigger vision of developing non-empirical/semi-empirical quantitative models to predict the dissolution behavior and chemical durability of glasses for various functional applications [170–172].

5. Conclusion

Through a multi-scale investigation of the impact of HFSCs on the dissolution behavior of borosilicate glasses in acidic media (pH = 2), we demonstrate here that HFSCs can impact the glass network significantly and thus lead to major changes in the dissolution kinetics, in both the forward rate and the long-term behavior, of the resultant glasses. While La³⁺ enhances the initial dissolution through nanoscale inhomogeneity of the glassy network, Nb⁵⁺, Zr⁴⁺ and Ti⁴⁺ tend to increase the chemical durability of the glass in the forward rate regime by increasing network connectivity and forming hydrolysis-resistant linkages (e.g., Si-O-Ti, Si-O-Zr and Si-O-Nb). However, for both HFSC-free and HFSC-containing samples, the transition towards the residual rate regime is heavily controlled by aqueous Si concentration near the glass surfacehence related to the Si reactivity—but not necessarily controlled by the presence of HFSC species near the glass surface. For instance, it is observed that although the limited solubility of Zr and Nb in acidic media enables the re-precipitation of Zr- and Nb-phases onto the glass surface, the as-formed nanoscale surface layers do not appear to have a passivating effect or influence the development of a silica passivating layer in our experimental duration. Instead, effective passivation can only be achieved after the formation and reorganization of a continuous amorphous silica layer as a result of local Si saturation near the glass-water interface. Therefore, slower initial dissolution does not necessarily guarantee enhanced long-term durability as it may delay the incorporation and

re-condensation of silica in the altered layer(s). As a result, to facilitate the design of functional glasses, compositions must be designed such that the dissolution kinetics in the forward and the residual rate regimes are properly balanced in accordance with expected glass lifetime requirements.

Additionally, while the fundamental mechanism that governs the dissolution of boro- and aluminoboro-silicate glass has been debated between IDPM and inter-diffusion-based mechanism in related literatures, our results highlight the possibility of a multiprocess acid-glass interaction that proceeds in a more complex manner than can be described by a single scenario. Depending on the reaction progress, different mechanisms may dominate the structural evolution within the altering glass.

We hope this work will complement the ongoing research attempting to decipher the fundamental chemistry governing the aqueous corrosion of borosilicate glasses and add to the quantitative composition – structure – property relationship database as in response to growing demands for a non-empirical model with which glass compositions can be designed with predictable dissolution behaviors.

Declaration of Competing Interest

The authors confirm the absence of any conflict of interest with this submission

The authors declare that they have no known competing financial interests or personal relationships that could have appeared to influence the work reported in this paper.

CRediT authorship contribution statement

Qianhui Qin: Conceptualization, Methodology, Data curation, Writing – original draft. **Nicholas Stone-Weiss:** Conceptualization, Methodology, Data curation, Writing – original draft. **Tongyao Zhao:** Data curation. **Pinaki Mukherjee:** Data curation. **Jinjun Ren:** Data curation. **John C. Mauro:** Conceptualization, Writing – original draft. **Ashutosh Goel:** Conceptualization, Writing – original draft.

Acknowledgment

This material is based upon work supported by the National Science Foundation under Grant No. 2034871. The Electron Microscopy research was performed at the Applied Chemical and Morphological Analysis Laboratory at Michigan Technological University (MTU), supported by NSF MRI 1429232. The Elastic Recoil Detection Analysis was performed at the Laboratory of Surface Modifications (LSM) at Rutgers University. The support from the China National Project titled, "Development and Verification of Two-Step Cold Crucible Vitrification Engineering-Scale Prototype" (Grant no. FKY1683ZHG001SSJS-B01-001) is acknowledged.

Supplementary materials

XRD patterns of the pre- and post-dissolution powders recovered from 28- and 120-days of corrosion; DSC thermograph of the un-corrded La-5 glass; FTIR spectrum of the studied glasses before and after dissolution; XPS survey spectrum of the corroded Zr-5 glass monolith; SEM-HAADF image and EDS elemental maps of recovered glass monolith for each studied composition; pH, ICP-OES readings, normalized loss and fraction of alteration data from all dissolution experiments.

Supplementary material associated with this article can be found, in the online version, at doi:10.1016/j.actamat.2022.118468.

References

- [1] Carlson, K.; Hart, S.; Nguyen, K.; Sabia, R.; Sternquist, D.; Zhang, L. Glass having anti-glare surface and method of making. US 8 771 532 B2, 2014.
- [2] Carleton, T.; Dabich, L.; Deneka, D.; Kanungo, M.; Li, S.; Mi, X.; Quesada, M.; Senaratne, W.; Speeckaert, J.; Stempin, L.; Walczak, W.; Woldegiworgis, H. Methods of making a glass article with a structured surface. US 2020/0002224 A1, 2020.
- [3] Hamilton, J.; Koch, K.; Li, A.; Mis, J.; Ravichandran, V.; Smith, N.; Wolcott, C.; Yongsunthon, R. Textured surfaces for display applications. US 10 698 151 B2, 2020
- [4] Agnello, G.; Jing, H.; Wolcott, C. Textured glass surfaces for reduced electrostatic charging. US 2020/0407274 A1, 2020.
- [5] Cavuoti, J.; Clark, D.; Garner, S.; Glaesemann, G.; Hou, J.; Kim, J.; Ono, T.; Sternquist, D. Surface flaw modification for strengthening of glass articles. US 9 315 412 B2 2016
- [6] L. Trotignon, J.C. Petit, G. Della Mea, J.C. Dran, The compared aqueous corrosion of four simple borosilicate glasses: influence of Al, Ca and Fe on the formation and nature of secondary phases, J. Nucl. Mater. 190 (1992) 228–246, doi:10.1016/0022-3115(92)90088-3.
- [7] C. Cailleteau, F. Angeli, F. Devreux, S. Gin, J. Jestin, P. Jollivet, O. Spalla, Insight into silicate-glass corrosion mechanisms, Nat. Mater. 7 (2008) 978, doi:10.1038/nmat2301.
- [8] A. Tournié, P. Ricciardi, P. Colomban, Glass corrosion mechanisms: a multiscale analysis, Solid State Ion. 179 (2008) 2142–2154, doi:10.1016/j.ssi.2008. 07.019
- [9] B. Bergeron, L. Galoisy, P. Jollivet, F. Angeli, T. Charpentier, G. Calas, S. Gin, First investigations of the influence of IVB elements (Ti, Zr, and Hf) on the chemical durability of soda-lime borosilicate glasses, J. NonCryst. Solids 356 (2010) 2315–2322, doi:10.1016/j.jnoncrysol.2010.07.065.
- [10] F. Angeli, M. Gaillard, P. Jollivet, T. Charpentier, Influence of glass composition and alteration solution on leached silicate glass structure: a solid-state NMR investigation, Geochim. Cosmochim. Acta 70 (2006) 2577–2590, doi:10.1016/ i.gca.2006.02.023.
- [11] S. Gin, X. Beaudoux, F. Angéli, C. Jégou, N. Godon, Effect of composition on the short-term and long-term dissolution rates of ten borosilicate glasses of increasing complexity from 3 to 30 oxides, J. NonCryst. Solids 358 (2012) 2559– 2570, doi:10.1016/j.jnoncrysol.2012.05.024.
- [12] H. Zhang, C.L. Corkhill, P.G. Heath, R.J. Hand, M.C. Stennett, N.C. Hyatt, Effect of Zn- and Ca-oxides on the structure and chemical durability of simulant alkali borosilicate glasses for immobilisation of UK high level wastes, J. Nucl. Mater. 462 (2015) 321–328, doi:10.1016/j.jnucmat.2015.04.016.
- [13] S. Mercado-Depierre, F. Angeli, F. Frizon, S. Gin, Antagonist effects of calcium on borosilicate glass alteration, J. Nucl. Mater. 441 (2013) 402–410, doi:10. 1016/j.jnucmat.2013.06.023.
- [14] J. Hopf, S.N. Kerisit, F. Angeli, T. Charpentier, J.P. Icenhower, B.P. McGrail, C.F. Windisch, S.D. Burton, E.M. Pierce, Glass-water interaction: effect of highvalence cations on glass structure and chemical durability, Geochim. Cosmochim. Acta 181 (2016) 54–71, doi:10.1016/j.gca.2016.02.023.
- [15] M. Ren, J.Y. Cheng, S.P. Jaccani, S. Kapoor, R.E. Youngman, L. Huang, J. Du, A. Goel, Composition structure property relationships in alkali aluminosilicate glasses: a combined experimental computational approach towards designing functional glasses, J. NonCryst. Solids 505 (2019) 144–153, doi:10.1016/j.jnoncrysol.2018.10.053.
- [16] J.P. Hamilton, S.L. Brantley, C.G. Pantano, L.J. Criscenti, J.D. Kubicki, Dissolution of nepheline, jadeite and albite glasses: toward better models for aluminosilicate dissolution, Geochim. Cosmochim. Acta 65 (2001) 3683–3702, doi:10.1016/S0016-7037(01)00724-4.
- [17] J.P. Hamilton, C.G. Pantano, S.L. Brantley, Dissolution of albite glass and crystal, Geochim. Cosmochim. Acta 64 (2000) 2603–2615, doi:10.1016/ S0016-7037(00)00388-4.
- [18] J.P. Hamilton, C.G. Pantano, Effects of glass structure on the corrosion behavior of sodium-aluminosilicate glasses, J. NonCryst. Solids 222 (1997) 167–174, doi:10.1016/S0022-3093(97)90110-1.
- [19] N. Stone-Weiss, R.E. Youngman, R. Thorpe, N.J. Smith, E.M. Pierce, A. Goel, An insight into the corrosion of alkali aluminoborosilicate glasses in acidic environments, Phys. Chem. Chem. Phys. 22 (2020) 1881–1896, doi:10.1039/ c9cp06064b.
- [20] T. Geisler, A. Janssen, D. Scheiter, T. Stephan, J. Berndt, A. Putnis, Aqueous corrosion of borosilicate glass under acidic conditions: a new corrosion mechanism, J. NonCryst. Solids 356 (2010) 1458–1465, doi:10.1016/j.jnoncrysol.2010. 04 033
- [21] E.H. Oelkers, S.R. Gislason, The mechanism, rates and consequences of basaltic glass dissolution: I. An experimental study of the dissolution rates of basaltic glass as a function of aqueous Al, Si and oxalic acid concentration at 25°C and pH = 3 and 11, Geochim. Cosmochim. Acta 65 (2001) 3671–3681, doi:10. 1016/s0016-7037(01)00664-0.
- [22] W. Vogel, N. Kreidl, M.L Barreto, Glass Chemistry, Springer Berlin, Heidelberg, 2012.
- [23] X. Lu, L. Deng, S. Gin, J. Du, Quantitative Structure–Property Relationship (QSPR) analysis of ZrO₂-containing soda-lime borosilicate glasses, J. Phys. Chem. B 123 (2019) 1412–1422, doi:10.1021/acs.jpcb.8b11108.
- [24] H. Wu, C. Lin, P. Shen, Structure and dissolution of $CaO-ZrO_2-TiO_2-Al_2O_3-B_2O_3-SiO_2$ glass (II), J. NonCryst. Solids 209 (1997) 76–86, doi:10.1016/s0022-3093(96)00553-4.

[25] A. Goel, E.R. Shaaban, F.C.L. Melo, M.J. Ribeiro, J.M.F Ferreira, Non-isothermal crystallization kinetic studies on MgO-Al₂O₃-SiO₂-TiO₂ glass, J. NonCryst. Solids 353 (2007) 2383–2391, doi:10.1016/j.jnoncrysol.2007.04.008.

- [26] D.S. Brauer, N. Karpukhina, R.V. Law, R.G. Hill, Effect of TiO₂ addition on structure, solubility and crystallisation of phosphate invert glasses for biomedical applications, J. NonCryst. Solids 356 (2010) 2626–2633, doi:10. 1016/j.jnoncrysol.2010.03.022.
- [27] M. Ma, W. Ni, Y. Wang, Z. Wang, F. Liu, The effect of TiO₂ on phase separation and crystallization of glass-ceramics in CaO-MgO-Al₂O₃-SiO₂-Na₂O system, J. NonCryst. Solids 354 (2008) 5395-5401, doi:10.1016/j.jnoncrysol.2008. 09 019
- [28] E.T. Nienhuis, J. Marcial, T. Robine, C. Le Losq, D.R. Neuville, M.C. Stennett, N.C. Hyatt, J.S. McCloy, Effect of Ti⁴⁺ on the structure of nepheline (NaAlSiO₄) glass, Geochim. Cosmochim. Acta 290 (2020) 333–351, doi:10.1016/j.gca.2020. 09.015
- [29] L. Cormier, G. Calas, D.R. Neuville, R. Bellissent, A high temperature neutron diffraction study of a titanosilicate glass, J. NonCryst. Solids 293 (2001) 510– 516, doi:10.1016/s0022-3093(01)00764-5.
- [30] X.C. Yang, M. Dubiel, D. Ehrt, A. Schütz, X-ray absorption near edge structure analysis of valence state and coordination geometry of Ti ions in borosilicate glasses, J. NonCryst. Solids 354 (2008) 1172–1174, doi:10.1016/j.jnoncrysol. 2006 11034
- [31] C. Cailleteau, F. Devreux, O. Spalla, F. Angeli, S. Gin, Why do certain glasses with a high dissolution rate undergo a low degree of corrosion? J. Phys. Chem. C 115 (2011) 5846-5855, doi:10.1021/jp111458f.
- [32] E. Pèlegrin, G. Calas, P. Ildefonse, P. Jollivet, L. Galoisy, Structural evolution of glass surface during alteration: application to nuclear waste glasses, J. NonCryst. Solids 356 (2010) 2497–2508, doi:10.1016/j.jinoncrysol. 2010.02.022.
- [33] P. Jollivet, L. Galoisy, G. Calas, F. Angeli, S. Gin, M.P. Ruffoni, N. Trcera, Zirconium local environment in simplified nuclear glasses altered in basic, neutral or acidic conditions: evidence of a double-layered gel, J. NonCryst. Solids 503-504 (2019) 268–278, doi:10.1016/j.jnoncrysol.2018.10.002.
- [34] R.D. Shannon, Revised effective ionic radii and systematic studies of interatomic distances in halides and chalcogenides, Acta Crystallogr. Sect. A 32 (1976) 751–767, doi:10.1107/s0567739476001551.
- [35] M. Fabian, F. Gergely, J. Osan, T. Cendak, S. Kesari, R. Rao, Structural investigation of borosilicate glasses containing lanthanide ions, Sci. Rep. 10 (2020) 7835, doi:10.1038/s41598-020-64754-2.
- [36] D.S. Patil, M. Konale, M. Gabel, O.K. Neill, J.V. Crum, A. Goel, M.C. Stennett, N.C. Hyatt, J.S. McCloy, Impact of rare earth ion size on the phase evolution of MoO₃-containing aluminoborosilicate glass-ceramics, J. Nucl. Mater. 510 (2018) 539–550, doi:10.1016/j.jnucmat.2018.08.004.
- [37] A. Brehault, D. Patil, H. Kamat, R.E. Youngman, L.M. Thirion, J.C. Mauro, C.L. Corkhill, J.S. McCloy, A. Goel, Compositional dependence of solubility/retention of molybdenum oxides in aluminoborosilicate-based model nuclear waste glasses, J. Phys. Chem. B 122 (2018) 1714–1729, doi:10.1021/acs. ipcb/7b09158
- [38] L. Dong, M. E. Fermann, H. McKay, L. Fu, S. Suzuki, Highly rare-earth-doped optical fibers for fiber lasers and amplifiers, US 8902493 B2 (2014).
- [39] M.J. Dejneka, B.Z. Hanson, S.G. Crigler, L.A. Zenteno, J.D. Minelly, D.C. Allan, W.J. Miller, D. Kuksenkov, La₂O₃-Al₂O₃-SiO₂ glasses for high-power, Yb³⁺-doped, 980-nm fiber lasers, J. Am. Ceram. Soc. 85 (2002) 1100–1106, doi:10. 1111/j.1151-2916.2002.tb00229.x.
- [40] S. Tanabe, K. Hirao, N. Soga, Elastic properties and molar volume of rare-earth aluminosilicate glasses, J. Am. Ceram. Soc. 75 (1992) 503–506, doi:10.1111/j. 1151-2916.1992.tb07833.x.
- [41] M.X. Qian, L.Y. Li, H. Li, D.M. Strachan, Partitioning of gadolinium and its induced phase separation in sodium-aluminoborosilicate glasses, J. NonCryst. Solids 333 (2004) 1–15, doi:10.1016/j.jnoncrysol.2003.09.056.
- [42] M.X. Qian, H. Li, L.Y. Li, D.M. Strachan, Extended electron energy loss fine structure simulation of the local boron environment in sodium aluminoborosilicate glasses containing gadolinium, J. NonCryst. Solids 328 (2003) 90–101, doi:10.1016/s0022-3093(03)00477-0.
- [43] L.Y. Li, H. Li, M.X. Qian, D.M. Strachan, Gadolinium solubility in peralkaline borosilicate glasses, J. NonCryst. Solids 283 (2001) 237–245, doi:10.1016/ s0022-3093(01)00480-x.
- [44] H. Kamat, F. Wang, K.E. Barnsley, J.V. Hanna, A.M. Tyryshkin, A. Goel, Insight into the partitioning and clustering mechanism of rare-earth cations in alkali aluminoborosilicate glasses, Chem. Mater. 33 (2021) 7944–7963, doi:10.1021/ acs.chemmater.1c01352.
- [45] T. Schaller, J.F. Stebbins, The structural role of lanthanum and yttrium in aluminosilicate glasses: a 27 Al and 17 O MAS NMR study, J. Phys. Chem. B 102 (1998) 10690–10697, doi:10.1021/jp982387m.
- [46] F. Angeli, T. Charpentier, E. Molières, A. Soleilhavoup, P. Jollivet, S. Gin, Influence of lanthanum on borosilicate glass structure: a multinuclear MAS and MQMAS NMR investigation, J. NonCryst. Solids 376 (2013) 189–198, doi:10.1016/j.inoncrysol.2013.05.042.
- [47] E. Molières, F. Angeli, P. Jollivet, S. Gin, T. Charpentier, O. Majérus, P. Barboux, D. de Ligny, O. Spalla, Chemical durability of lanthanum-enriched borosilicate glass, Int. J. Appl. Glass Sci. 4 (2013) 383–394, doi:10.1111/jjag.12054.
- [48] J. Cao, B. Poumellec, L. Mazerolles, F. Brisset, A.-L. Helbert, S. Surble, X. He, M. Lancry, Nanoscale phase separation in lithium niobium silicate glass by femtosecond laser irradiation, J. Am. Ceram. Soc. 100 (2017) 115–124, doi:10. 1111/jace.14570.

[49] A. Herczog, Phase distribution and transparency in glass-ceramics based on a study of the sodium niobate-silica system, J. Am. Ceram. Soc. 73 (1990) 2743–2746, doi:10.1111/j.1151-2916.1990.tb06756.x.

- [50] C.R. Gautam, D. Kumar, O. Parkash, Controlled crystallization of (Pb, Sr)TiO₃ borosilicate glass ceramics doped with Nb₂O₅, Glass Phys. Chem. 39 (2013) 162–173, doi:10.1134/s1087659613020089.
- [51] Q. Zhang, X. Du, S. Tan, D. Tang, K. Chen, T. Zhang, Effect of Nb_2O_5 doping on improving the thermo-mechanical stability of sealing interfaces for solid oxide fuel cells, Sci. Rep. 7 (2017) 5355, doi:10.1038/s41598-017-05725-y.
- [52] R.C.C. Monteiro, A.A.S. Lopes, M.M.R.A. Lima, J.P.B Veiga, Thermal characteristics and crystallization behavior of zinc borosilicate glasses containing Nb₂O₅, J. NonCryst. Solids 491 (2018) 124–132, doi:10.1016/j.inoncrysol.2018.03.054.
- [53] K. Fukumi, S. Sakka, Coordination state of Nb⁵⁺ ions in silicate and gallate glasses as studied by Raman spectroscopy, J. Mater. Sci. 23 (1988) 2819–2823, doi:10.1007/bf00547456.
- [54] M.P.F. Graça, M.G. Ferreira da Silva, M.A. Valente, NaNbO₃ crystals dispersed in a B₂O₃ glass matrix—structural characteristics versus electrical and dielectrical properties, Solid State Sci. 11 (2009) 570–577, doi:10.1016/j. solidstatesciences.2008.07.010.
- [55] E.V. Kolobkova, Coordination states of niobium and its structural role in lanthanum borate glasses according to data from vibrational spectroscopy, Fiz Khim, Stekal 14 (1988) 490–493.
- [56] B. Samuneva, S. Kralchev, V. Dimitrov, Structure and optical properties of niobium silicate glasses, J. NonCryst. Solids 129 (1991) 54–63, doi:10.1016/ 0022-3093(91)90080-p.
- [57] L.F. Santos, L. Wondraczek, J. Deubener, R.M. Almeida, Vibrational spectroscopy study of niobium germanosilicate glasses, J. NonCryst. Solids 353 (2007) 1875–1881, doi:10.1016/j.jnoncrysol.2007.02.018.
- [58] A. Aronne, V.N. Sigaev, B. Champagnon, E. Fanelli, V. Califano, L.Z. Usmanova, P. Pernice, The origin of nanostructuring in potassium niobiosilicate glasses by Raman and FTIR spectroscopy, J. NonCryst. Solids 351 (2005) 3610–3618, doi:10.1016/j.jnoncrysol.2005.09.019.
- [59] Mazurin, O.; Streltsina, M.; Shvaiko-Shvaikovskaya, T. Sci Glass-6.5 (Glass Property Information System). Institute of Theoretical Chemistry, Shrewsbury, MA, USA 2005,
- [60] D. Massiot, F. Fayon, M. Capron, I. King, S. Le Calvé, B. Alonso, J.-O. Durand, B. Bujoli, Z. Gan, G. Hoatson, Modelling one- and two-dimensional solid-state NMR spectra, Magn. Reson. Chem. 40 (2002) 70-76, doi:10.1002/mrc.984.
- [61] D. Massiot, C. Bessada, J.P. Coutures, F. Taulelle, A quantitative study of ²⁷Al MAS NMR in crystalline YAG, J. Magn. Reson. 90 (1990) 231–242 (1969), doi:10.1016/0022-2364(90)90130-2.
- [62] F. Wang, N. Balasubramanya, Q. Qin, R.E. Youngman, P. Mukherjee, N. Stone-Weiss, A. Goel, Multiscale investigation of the mechanisms controlling the corrosion of borosilicate glasses in hyper-alkaline media, J. Phys. Chem. C 124 (2020) 27542–27557, doi:10.1021/acs.jpcc.0c08691.
- [63] ASTM International. Standard Test Method for Static Leaching of Monolithic Waste Forms for Disposal of Radioactive Waste; ASTM C-1220-98/XAB; West Conshohocken, PA, 1998.
- [64] J.H. Scofield, Theoretical Photoionization Cross Sections from 1 to 1500 keV, Lawrence Livermore National Laboratory, Livermore, CA, 1973, doi:10.2172/ 4545040.
- [65] G.C. Smith, Evaluation of a simple correction for the hydrocarbon contamination layer in quantitative surface analysis by XPS, J. Electron Spectrosc. Relat. Phenom. 148 (2005) 21–28, doi:10.1016/j.elspec.2005.02.004.
- [66] T. Gullion, J. Schaefer, Rotational-echo double-resonance NMR, J. Magn. Reson. 81 (1989) (1969), doi:10.1016/0022-2364(89)90280-1.
- [67] L.J. Allen, A.J. D'Alfonso, B. Freitag, D.O. Klenov, Chemical mapping at atomic resolution using energy-dispersive x-ray spectroscopy, MRS Bull. 37 (2012) 47–52, doi:10.1557/mrs.2011.331.
- [68] F. Angeli, T. Charpentier, M. Gaillard, P. Jollivet, Influence of zirconium on the structure of pristine and leached soda-lime borosilicate glasses: towards a quantitative approach by ¹⁷O MQMAS NMR, J. NonCryst. Solids 354 (2008) 3713–3722, doi:10.1016/j.jnoncrysol.2008.03.046.
- [69] L. Galoisy, E. Pélegrin, M.-A. Arrio, P. Ildefonse, G. Calas, D. Ghaleb, C. Fillet, F. Pacaud, Evidence for 6-coordinated zirconium in inactive nuclear waste glasses, J. Am. Ceram. Soc. 82 (1999) 2219–2224, doi:10.1111/j.1151-2916.1999. tb02065 x
- [70] R. Limbach, S. Karlsson, G. Scannell, R. Mathew, M. Edén, L. Wondraczek, The effect of TiO₂ on the structure of Na₂O-CaO-SiO₂ glasses and its implications for thermal and mechanical properties, J. NonCryst. Solids 471 (2017) 6–18, doi:10.1016/j.jinoncrysol.2017.04.013.
- [71] F. Angeli, T. Charpentier, D. De Ligny, C. Cailleteau, Boron speciation in sodalime borosilicate glasses containing zirconium, J. Am. Ceram. Soc. 93 (2010) 2693–2704, doi:10.1111/j.1551-2916.2010.03771.x.
- [72] S.K. Lee, J.F. Stebbins, Nature of cation mixing and ordering in Na-Ca silicate glasses and melts, J. Phys. Chem. B 107 (2003) 3141–3148, doi:10.1021/in027489v
- [73] J. Wu, J.F. Stebbins, Effects of cation field strength on the structure of aluminoborosilicate glasses: high-resolution ¹¹B, ²⁷Al and ²³Na MAS NMR, J. Non-Cryst. Solids 355 (2009) 556–562, doi:10.1016/j.jnoncrysol.2009.01.025.
- [74] T.K. Bechgaard, A. Goel, R.E. Youngman, J.C. Mauro, S.J. Rzoska, M. Bockowski, L.R. Jensen, M.M. Smedskjaer, Structure and mechanical properties of compressed sodium aluminosilicate glasses: role of non-bridging oxygens, J. Non-Cryst. Solids 441 (2016) 49–57, doi:10.1016/j.jnoncrysol.2016.03.011.

- [75] S. Sen, Z. Xu, J.F. Stebbins, Temperature dependent structural changes in borate, borosilicate and boroaluminate liquids: high-resolution 11B, 29Si and ²⁷Al NMR studies, J. NonCryst. Solids 226 (1998) 29-40, doi:10.1016/ s0022-3093(97)00491-2.
- [76] L.-S. Du, J.F. Stebbins, Nature of silicon-boron mixing in sodium borosilicate glasses: a high-resolution ¹¹B and ¹⁷O NMR study, J. Phys. Chem. B 107 (2003) 10063-10076, doi:10.1021/jp0340481.
- L.-S. Du, J.F. Stebbins, Site preference and Si/B mixing in mixed-alkali borosilicate glasses: a high-resolution ¹¹B and ¹⁷O NMR study, Chem. Mater. 15 (2003) 3913-3921, doi:10.1021/cm034427r.
- [78] E.I. Morin, J. Wu, J.F. Stebbins, Modifier cation (Ba, Ca, La, Y) field strength effects on aluminum and boron coordination in aluminoborosilicate glasses: the roles of fictive temperature and boron content, Appl. Phys. A 116 (2014) 479-490, doi:10.1007/s00339-014-8369-4
- [79] G.S. Henderson, X. Liu, M.E. Fleet, A Ti L-edge X-ray absorption study of Ti-silicate glasses, Phys. Chem. Miner. 29 (2002) 32-42, doi:10.1007/ s002690100208.
- [80] M.R. Ackerson, G.D. Cody, B.O Mysen, $^{29}\mathrm{Si}$ solid state NMR and Ti K-edge XAFS pre-edge spectroscopy reveal complex behavior of Ti in silicate melts, Prog. Earth Planet. Sci. 7 (2020) 14, doi:10.1186/s40645-020-00326-2.
- T.H. Elmer, M.E. Nordberg, Solubility of silica in nitric acid solutions, J. Am. Ceram. Soc. 41 (1958) 517-520, doi:10.1111/j.1151-2916.1958.tb12907.x
- J. Kragten, Tutorial review. Calculating standard deviations and confidence intervals with a universally applicable spreadsheet technique, Analyst 119 (1994) 2161-2165, doi:10.1039/an9941902161.
- M. Fournier, A. Ull, E. Nicoleau, Y. Inagaki, M. Odorico, P. Frugier, S. Gin, Glass dissolution rate measurement and calculation revisited, J. Nucl. Mater. 476 (2016) 140-154, doi:10.1016/j.jnucmat.2016.04.028.
- B.C. Bunker, G.W. Arnold, D.E. Day, P. Bray, The effect of molecular structure on borosilicate glass leaching, J. NonCryst. Solids 87 (1986) 226-253, doi:10. 1016/s0022-3093(86)80080-1.
- G. Ferlat, L. Cormier, M.H. Thibault, L. Galoisy, G. Calas, J.M. Delaye, D. Ghaleb, Evidence for symmetric cationic sites in zirconium-bearing oxide glasses, Phys. Rev. B 73 (2006) 214207, doi:10.1103/physrevb.73.214207
- G.A.C.M. Spierings, The influence of $\mbox{Nb}_2\mbox{O}_5$ on the properties of sodium borosilicate glass, J. NonCryst. Solids 47 (1982) 421-425, doi:10.1016/ 0022-3093(82)90218-6.
- T. Yajima, S. Tobita, S. Ueta, Solubility measurement of niobium in the system Nb-OH under CO₂-free conditions, in: Proceedings of 1992 Fall Meeting of the Atomic Energy Society of Japan, Nagoya, Japan, 1992.
- C. Peiffert, C. Nguyen-Trung, D.A. Palmer, J.P. Laval, E. Giffaut, Solubility of B-Nb₂O₅ and the hydrolysis of niobium(V) in aqueous solution as a function of temperature and ionic strength, J. Solut. Chem. 39 (2010) 197-218, doi:10. 1007/s10953-010-9495-z.
- K.T. Jacob, C. Shekhar, M. Vinay, Y. Waseda, Thermodynamic properties of niobium oxides, J. Chem. Eng. Data 55 (2010) 4854-4863, doi:10.1021/je1004609.
- [90] J.D. Rimstidt, H.L. Barnes, The kinetics of silica-water reactions, Geochim. Cosmochim. Acta 44 (1980) 1683–1699, doi:10.1016/0016-7037(80)90220-3
- J. Schmidt, W. Vogelsberger, Dissolution kinetics of titanium dioxide nanoparticles: the observation of an unusual kinetic size effect, J. Phys. Chem. B 110 (2006) 3955-3963, doi:10.1021/jp0553611.
- [92] W. Zouari, T. Suzuki-Muresan, T. Kobayashi, S. Utsunomiya, A. Abdelouas, B. Grambow, Solubility of monoclinic and yttrium stabilized cubic ZrO2: solution and surface thermodynamics guiding ultra-trace analytics in aqueous phase, J. Nucl. Mater. 545 (2021) 152631, doi:10.1016/j.jnucmat.2020.152631.
- [93] H.A. Elbatal, M.A. Azooz, E.A. Saad, F.M. EzzEldin, M.S. Amin, Corrosion behavior mechanism of borosilicate glasses towards different leaching solutions evaluated by the grain method and FTIR spectral analysis before and after gamma irradiation, Silicon 10 (2018) 1139-1149, doi:10.1007/ s12633-017-9586-1.
- [94] S. Peng, Z. Ke, X. Cao, C. Shan, F. Zhao, M. Guan, L. Shi, Y. Sun, Y. Yang, L. Ma, A novel type of borosilicate glass with excellent chemical stability and high ultraviolet transmission, J. NonCryst. Solids 528 (2020) 119735, doi:10.1016/j. inoncrysol.2019.119735.
- [95] A.M. Efimov, Vibrational spectra, related properties, and structure of inorganic glasses, J. NonCryst. Solids 253 (1999) 95-118, doi:10.1016/S0022-3093(99)
- [96] S.M. Abo-Naf, F.H. El Batal, M.A. Azooz, Characterization of some glasses in the system SiO2, Na2O RO by infrared spectroscopy, Mater. Chem. Phys. 77 (2003) 846-852, doi:10.1016/S0254-0584(02)00215-8.
- A.C. Lee, S.K. Lee, Effect of composition on structural evolution and NMR parameters of quadrupolar nuclides in sodium borate and aluminoborosilicate glasses: a view from high-resolution ¹¹B, ²⁷Al, and ¹⁷O solid-state NMR, J. NonCryst. Solids 555 (2021) 120271, doi:10.1016/j.jnoncrysol.2020.120271.
- S. Ghose, T. Tsang, Structural dependence of quadrupole coupling constant e²qQ/h for ²⁷Al and crystal field parameter D for Fe³⁺ in aluminosilicates, Am. Mineral. 58 (1973) 748-755.
- [99] G. Engelhardt, D. Michel, High-resolution solid-state NMR of silicates and zeolites, Wiley, 1988.
- [100] B. Walkley, A. Kashani, M.-A. Sani, T.D. Ngo, P. Mendis, Examination of alkaliactivated material nanostructure during thermal treatment, J. Mater. Sci. 53 (2018) 9486-9503, doi:10.1007/s10853-018-2270-z.
- [101] M.L. Balmer, B.C. Bunker, L.Q. Wang, C.H.F. Peden, Y. Su, Solid-state ²⁹Si MAS NMR study of titanosilicates, J. Phys. Chem. B 101 (1997) 9170-9179, doi:10. 1021/ip971429o.

[102] S.W. Martin, A. Bhatnagar, C. Parameswar, S. Feller, J. MacKenzie, ²⁹Si MAS-NMR study of the short-range order in potassium borosilicate glasses, J. Am. Ceram. Soc. 78 (1995) 952–960, doi:10.1111/j.1151-2916.1995.tb08421.x.

- [103] L. van Wüllen, W. Müller-Warmuth, D. Papageorgiou, H.J. Pentinghaus, Characterization and structural developments of gel-derived borosilicate glasses: a multinuclear MAS-NMR study, J. NonCryst. Solids 171 (1994) 53-67, doi:10. 1016/0022-3093(94)90032-9.
- [104] V. Eremyashev, L.M. Osipova, I. Shenderovich, The effects of alkaline earth metals on the structure of sodium borosilicate glasses: ¹¹B and ²⁹Si NMR study, Mater. Sci. Forum 989 (2020) 192-198, doi:10.4028/www.scientific.net/ msf.989.192.
- [105] G.S. Henderson, M.E. Fleet, The structure of Ti silicate glasses by micro-Raman
- spectroscopy, Can. Mineral. 33 (1995) 399–408.

 [106] I.S. Protsak, Y.M. Morozov, W. Dong, Z. Le, D. Zhang, I.M. Henderson, A ²⁹Si,

 ¹H, and ¹³C solid-state NMR study on the surface species of various depolymerized organosiloxanes at silica surface, Nanoscale Res. Lett. 14 (2019) 160, doi:10.1186/s11671-019-2982-2.
- [107] M.S. Bødker, R.E. Youngman, J.C. Mauro, M.M. Smedskjaer, Mixed alkali effect in silicate glass structure: viewpoint of ²⁹Si nuclear magnetic resonance and statistical mechanics, J. Phys. Chem. B 124 (2020) 10292–10299, doi:10.1021/ acs.ipcb.0c07980.
- [108] J.H. Baltisberger, P. Florian, E.G. Keeler, P.A. Phyo, K.J. Sanders, P.J. Grandinetti, Modifier cation effects on ²⁹Si nuclear shielding anisotropies in silicate glasses, J. Magn. Reson. 268 (2016) 95–106, doi:10.1016/j.jmr.2016.05.003.
- [109] S.C. Kohn, R. Dupree, M.E. Smith, Proton environments and hydrogen-bonding in hydrous silicate glasses from proton NMR, Nature 337 (1989) 539-541, doi:10.1038/337539a0.
- [110] T. Schaller, A. Sebald, One- and two-dimensional ¹H magic-angle spinning experiments on hydrous silicate glasses, Solid State Nucl. Magn. Reson. 5 (1995) 89-102, doi:10.1016/0926-2040(95)00028-o.
- [111] Q. Zeng, H. Nekvasil, C.P. Grey, Proton environments in hydrous aluminosilicate glasses: a 1 H MAS, 1 H/ 2 7Al, and 1 H/ 2 8Na TRAPDOR NMR study, J. Phys. Chem. B 103 (1999) 7406-7415, doi:10.1021/jp9907261.
- [112] W.J. Malfait, X. Xue, The nature of hydroxyl groups in aluminosilicate glasses: quantifying Si-OH and Al-OH abundances along the SiO_2 -NaAlSiO₄ join by ¹H, ²⁷Al-¹H and ²⁹Si-¹H NMR spectroscopy, Geochim. Cosmochim. Acta 74 (2010) 719-737, doi:10.1016/j.gca.2009.10.036.
- [113] B.C. Bunker, D.R. Tallant, T.J. Headley, G.L. Turner, R.J. Kirkpatrick, The structure of leached sodium borosilicate glass, Phys. Chem. Glasses 29 (1988) 106-120.
- [114] V. Simon, M. Todea, A.F. Takács, M. Neumann, S. Simon, XPS study on silicabismuthate glasses and glass ceramics, Solid State Commun. 141 (2007) 42-47, doi:10.1016/j.ssc.2006.09.036.
- [115] J. Serra, P. González, S. Liste, C. Serra, S. Chiussi, B. León, M. Pérez-Amor, H.O. Ylänen, M. Hupa, FTIR and XPS studies of bioactive silica based glasses, J. NonCryst. Solids 332 (2003) 20-27, doi:10.1016/j.jnoncrysol.2003.09.013.
- [116] B.M.J. Smets, T.P.A Lommen, The structure of germanosilicate glasses, studied by X-ray photoelectron spectroscopy, J. NonCryst. Solids 46 (1981) 21-32, doi:10.1016/0022-3093(81)90071-5.
- [117] J. Banerjee, S.H. Kim, C.G. Pantano, Elemental areal density calculation and oxygen speciation for flat glass surfaces using x-ray photoelectron spectroscopy, J. NonCryst. Solids 450 (2016) 185-193, doi:10.1016/j.jnoncrysol.
- [118] J.F. Moulder, Handbook of X-Ray Photoelectron Spectroscopy: a Reference Book of Standard Spectra for Identification and Interpretation of XPS Data, Physical Electronics Division, Perkin-Elmer Corporation, 1992.
- [119] T. Gross, M. Ramm, H. Sonntag, W. Unger, H.M. Weijers, E.H. Adem, An XPS analysis of different SiO₂ modifications employing a C 1s as well as an Au 4f_{7/2} static charge reference, Surf. Interface Anal. 18 (1992) 59-64, doi:10.1002/sia.740180110.
- [120] Y. Miura, H. Kusano, T. Nanba, S. Matsumoto, X-ray photoelectron spectroscopy of sodium borosilicate glasses, J. NonCryst. Solids 290 (2001) 1-14, doi:10.1016/s0022-3093(01)00720-7.
- [121] R.M. Palomino, R.A. Gutiérrez, Z. Liu, S. Tenney, D.C. Grinter, E. Crumlin, I. Waluyo, P.J. Ramírez, J.A. Rodriguez, S.D. Senanayake, Inverse catalysts for CO oxidation: enhanced oxide-metal interactions in MgO/Au(111), CeO₂/Au(111), and TiO₂/Au(111), ACS Sustain. Chem. Eng. 5 (2017) 10783-10791, doi:10.1021/acssuschemeng.7b02744.
- [122] F. Chen, H. Yang, K. Li, B. Deng, Q. Li, X. Liu, B. Dong, X. Xiao, D. Wang, Y. Qin, S.-M. Wang, K.-Q. Zhang, W. Xu, Facile and effective coloration of dye-inert carbon fiber fabrics with tunable colors and excellent laundering durability, ACS Nano 11 (2017) 10330-10336, doi:10.1021/acsnano.7b05139.
- [123] B. Erdem, R.A. Hunsicker, G.W. Simmons, E.D. Sudol, V.L. Dimonie, M.S. El-Aasser, XPS and FTIR surface characterization of TiO₂ particles used in polymer encapsulation, Langmuir 17 (2001) 2664-2669, doi:10.1021/ la0015213.
- [124] J.A. Anderson, J.L.G Fierro, Bulk and surface properties of copper-containing oxides of the general formula $LaZr_{1-x}Cu_xO_3$, J. Solid State Chem. 108 (1994) 305-313, doi:10.1006/jssc.1994.1047
- [125] D. Majumdar, D. Chatterjee, X-ray photoelectron spectroscopic studies on yttria, zirconia, and yttria-stabilized zirconia, J. Appl. Phys. 70 (1991) 988-992, doi:10.1063/1.349611.
- [126] A.P. Dementjev, O.P. Ivanova, L.A. Vasilyev, A.V. Naumkin, D.M. Nemirovsky, D.Y. Shalaev, Altered layer as sensitive initial chemical state indicator, J. Vac. Sci. Technol. A 12 (1994) 423-427, doi:10.1116/1.579258.

[127] C. Morant, J.M. Sanz, L. Galán, L. Soriano, F. Rueda, An XPS study of the interaction of oxygen with zirconium, Surf. Sci. 218 (1989) 331–345, doi:10.1016/ 0039-6028(89)90156-8.

- [128] F. Garbassi, J.C.J. Bart, G. Petrini, XPS study of tellurium—niobium and tellurium—tantalum oxide systems, J. Electron Spectrosc. Relat. Phenom. 22 (1981) 95–107, doi:10.1016/0368-2048(81)80019-9.
- [129] N. Özer, D.-G. Chen, C.M. Lampert, Preparation and properties of spin-coated Nb₂O₅ films by the sol-gel process for electrochromic applications, Thin Solid Films 277 (1996) 162–168, doi:10.1016/0040-6090(95)08011-2.
- [130] D.D. Sarma, C.N.R. Rao, XPES studies of oxides of second- and third-row transition metals including rare earths, J. Electron Spectrosc. Relat. Phenom. 20 (1980) 25-45, doi:10.1016/0368-2048(80)85003-1.
- [131] M.A.B. Gomes, L.O.d.S. Bulhões, S.C. de Castro, A.J. Damião, The electrochromic process at Nb₂O₅ electrodes prepared by thermal oxidation of niobium, J. Electrochem. Soc. 137 (1990) 3067–3070, doi:10.1149/1.2086161.
- [132] S. Gin, X. Guo, J.-M. Delaye, F. Angeli, K. Damodaran, V. Testud, J. Du, S. Kerisit, S.H. Kim, Insights into the mechanisms controlling the residual corrosion rate of borosilicate glasses, NPJ Mater. Degrad. 4 (2020) 41, doi:10.1038/ s41529-020-00145-2.
- [133] S. Gin, P. Jollivet, M. Fournier, F. Angeli, P. Frugier, T. Charpentier, Origin and consequences of silicate glass passivation by surface layers, Nat. Commun. 6 (2015) 6360, doi:10.1038/ncomms7360.
- [134] S. Gin, M. Collin, P. Jollivet, M. Fournier, Y. Minet, L. Dupuy, T. Mahadevan, S. Kerisit, J. Du, Dynamics of self-reorganization explains passivation of silicate glasses, Nat. Commun. 9 (2018) 2169, doi:10.1038/s41467-018-04511-2.
- [135] S. Gin, A.H. Mir, A. Jan, J.M. Delaye, E. Chauvet, Y. De Puydt, A. Gourgiotis, S. Kerisit, A general mechanism for gel layer formation on borosilicate glass under aqueous corrosion, J. Phys. Chem. C 124 (2020) 5132–5144, doi:10.1021/ acs.jpcc.9b10491.
- [136] K. Furutani, T. Ohkubo, J. Du, K. Ohara, K. Deguchi, S. Ohki, T. Shimizu, Y. Inagaki, R. Matsubara, K. Ishida, Elucidating the atomic structures of the gel layer formed during aluminoborosilicate glass dissolution: an integrated experimental and simulation study, J. Phys. Chem. C 126 (2022) 7999–8015, doi:10.1021/acs.jpcc.1c10463.
- [137] T. Geisler, T. Nagel, M.R. Kilburn, A. Janssen, J.P. Icenhower, R.O.C. Fonseca, M. Grange, A.A. Nemchin, The mechanism of borosilicate glass corrosion revisited, Geochim. Cosmochim. Acta 158 (2015) 112–129, doi:10.1016/j.gca. 2015.02.039.
- [138] N. Tsomaia, S.L. Brantley, J.P. Hamilton, C.G. Pantano, K.T. Mueller, NMR evidence for formation of octahedral and tetrahedral Al and repolymerization of the Si network during dissolution of aluminosilicate glass and crystal, Am. Mineral. 88 (2003) 54–67, doi:10.2138/am-2003-0107.
- [139] J. Declercq, T. Diedrich, M. Perrot, S.R. Gislason, E.H. Oelkers, Experimental determination of rhyolitic glass dissolution rates at 40–200°C and 2 < pH < 10.1, Geochim. Cosmochim. Acta 100 (2013) 251–263, doi:10.1016/j.gca.2012. 10.006
- [140] D. Wolff-Boenisch, S.R. Gislason, E.H. Oelkers, C.V. Putnis, The dissolution rates of natural glasses as a function of their composition at pH 4 and 10.6, and temperatures from 25 to 74°C, Geochim. Cosmochim. Acta 68 (2004) 4843–4858, doi:10.1016/j.gca.2004.05.027.
- [141] D. Wolff-Boenisch, S.R. Gislason, E.H. Oelkers, The effect of fluoride on the dissolution rates of natural glasses at pH 4 and 25°C, Geochim. Cosmochim. Acta 68 (2004) 4571–4582, doi:10.1016/j.gca.2004.05.026.
- [142] S.R. Gislason, E.H. Oelkers, Mechanism, rates, and consequences of basaltic glass dissolution: II. An experimental study of the dissolution rates of basaltic glass as a function of pH and temperature, Geochim. Cosmochim. Acta 67 (2003) 3817–3832, doi:10.1016/S0016-7037(03)00176-5.
- [143] G. Berger, C. Claparols, C. Guy, V. Daux, Dissolution rate of a basalt glass in silica-rich solutions: implications for long-term alteration, Geochim. Cosmochim. Acta 58 (1994) 4875–4886, doi:10.1016/0016-7037(94)90218-6.
- [144] B. Cagnon, D. Daval, M. Cabié, D. Lemarchand, S. Gin, A comparative study of the dissolution mechanisms of amorphous and crystalline feldspars at acidic pH conditions, NPJ Mater. Degrad. 6 (2022) 34, doi:10.1038/ s41529-022-00240-6.
- [145] K.G. Knauss, W.L. Bourcier, K.D. McKeegan, C.I. Merzbacher, S.N. Nguyen, F.J. Ryerson, D.K. Smith, H.C. Weed, L. Newton, Dissolution kinetics of a simple analogue nuclear waste glass as a function of pH, time and temperature, MRS Proc. 176 (1989) 176, doi:10.1557/proc-176-176.
- [146] R. Jones, J. Stewart, The kinetics of corrosion of E-glass fibres in sulphuric acid, J. NonCryst. Solids 356 (2010) 2433–2436, doi:10.1016/j.jnoncrysol.2010. 07.062
- [147] Q. Qiu, M. Kumosa, Corrosion of E-glass fibers in acidic environments, Compos. Sci. Technol. 57 (1997) 497–507, doi:10.1016/s0266-3538(96)00158-3.
- [148] R.H. Doremus, Interdiffusion of hydrogen and alkali ions in a glass surface, J. NonCryst. Solids 19 (1975) 137–144, doi:10.1016/0022-3093(75)90079-4.

[149] B.C. Bunker, Molecular mechanisms for corrosion of silica and silicate glasses, J. NonCryst. Solids 179 (1994) 300–308, doi:10.1016/0022-3093(94)90708-0.

- [150] J. Hopf, J.R. Eskelsen, M. Chiu, A. Ievlev, O.S. Ovchinnikova, D. Leonard, E.M. Pierce, Toward an understanding of surface layer formation, growth, and transformation at the glass-fluid interface, Geochim. Cosmochim. Acta 229 (2018) 65-84, doi:10.1016/j.gca.2018.01.035.
- [151] J.D. Vienna, J.V. Ryan, S. Gin, Y. Inagaki, Current understanding and remaining challenges in modeling long-term degradation of borosilicate nuclear waste glasses, Int. J. Appl. Glass Sci. 4 (2013) 283–294, doi:10.1111/jjag.12050.
- [152] C. Lenting, O. Plümper, M. Kilburn, P. Guagliardo, M. Klinkenberg, T. Geisler, Towards a unifying mechanistic model for silicate glass corrosion, NPJ Mater. Degrad. 2 (2018) 28, doi:10.1038/s41529-018-0048-z.
- [153] S. Gin, L. Neill, M. Fournier, P. Frugier, T. Ducasse, M. Tribet, A. Abdelouas, B. Parruzot, J. Neeway, N. Wall, The controversial role of inter-diffusion in glass alteration, Chem. Geol. 440 (2016) 115–123, doi:10.1016/j.chemgeo.2016. 07.014.
- [154] R. Hellmann, S. Cotte, E. Cadel, S. Malladi, L.S. Karlsson, S. Lozano-Perez, M. Cabié, A. Seyeux, Nanometre-scale evidence for interfacial dissolutionreprecipitation control of silicate glass corrosion, Nat. Mater. 14 (2015) 307, doi:10.1038/nmat4172.
- [155] T. Geisler, L. Dohmen, C. Lenting, M.B.K Fritzsche, Real-time in situ observations of reaction and transport phenomena during silicate glass corrosion by fluid-cell Raman spectroscopy, Nat. Mater. 18 (2019) 342–348, doi:10.1038/ s41563-019-0293-8.
- [156] S.K. Lee, C.B. Musgrave, P. Zhao, J.F. Stebbins, Topological disorder and reactivity of borosilicate glasses: quantum chemical calculations and 170 and 11B NMR study, J. Phys. Chem. B 105 (2001) 12583–12595, doi:10.1021/jp012119f.
- [157] M. Fournier, T. Ducasse, A. Pérez, A. Barchouchi, D. Daval, S. Gin, Effect of pH on the stability of passivating gel layers formed on International Simple Glass, J. Nucl. Mater. 524 (2019) 21–38, doi:10.1016/j.jnucmat.2019.06.029.
- [158] J.C. Mauro, C.S. Philip, D.J. Vaughn, M.S. Pambianchi, Glass science in the United States: current status and future directions, Int. J. Appl. Glass Sci. 5 (2014) 2–15, doi:10.1111/jjag.12058.
- [159] J.C. Mauro, A. Tandia, K.D. Vargheese, Y.H.Z. Mauro, M.M. Smedskjaer, Accelerating the design of functional glasses through modeling, Chem. Mater. 28 (2016) 4267–4277, doi:10.1021/acs.chemmater.6b01054.
- [160] Q. Zheng, M. Potuzak, J.C. Mauro, M.M. Smedskjaer, R.E. Youngman, Y. Yue, Composition-structure-property relationships in boroaluminosilicate glasses, J. NonCryst. Solids 358 (2012) 993–1002, doi:10.1016/j.jnoncrysol.2012.01.030.
- [161] M.M. Smedskjaer, Q. Zheng, J.C. Mauro, M. Potuzak, S. Mørup, Y. Yue, Sodium diffusion in boroaluminosilicate glasses, J. NonCryst. Solids 357 (2011) 3744– 3750, doi:10.1016/j.jnoncrysol.2011.07.008.
- [162] L. Deng, J. Du, Development of effective empirical potentials for molecular dynamics simulations of the structures and properties of boroaluminosilicate glasses, J. NonCryst. Solids 453 (2016) 177–194, doi:10.1016/j.jnoncrysol.2016. 09.021
- [163] M.D.J. Auch, O.K. Soo, G. Ewald, C. Soo-Jin, Ultrathin glass for flexible OLED application, Thin Solid Films 417 (2002) 47–50, doi:10.1016/S0040-6090(02) 00647.8
- [164] A. Ellison, I.A. Cornejo, Glass substrates for liquid crystal displays, Int. J. Appl. Glass Sci. 1 (2010) 87–103, doi:10.1111/j.2041-1294.2010.00009.x.
- [165] G. Macrelli, A.K. Varshneya, J.C. Mauro, Ultra-thin glass as a substrate for flexible photonics, Opt. Mater. 106 (2020) 109994, doi:10.1016/j.optmat.2020. 109994
- [166] C.-T. Lee, Non-HF type etching solution for slimming of flat panel display glass, Appl. Chem. Eng. 27 (2016) 101–109, doi:10.14478/ace.2016.1005.
- [167] N.I. Min'ko, V.M. Nartsev, Effect of the glass composition on corrosion of zirconium-containing refractories in a glass-melting furnace (a review), Glass Ceram. 64 (2007) 335–342, doi:10.1007/s10717-007-0084-6.
- [168] K. Kato, N. Araki, The corrosion of zircon and zirconia refractories by molten glasses, J. NonCryst. Solids 80 (1986) 681–687, doi:10.1016/0022-3093(86) 90462-x.
- [169] K.S. Gerace, J.C. Mauro, C.A. Randall, Piezoelectric glass-ceramics: crystal chemistry, orientation mechanisms, and emerging applications, J. Am. Ceram. Soc. 104 (2021) 1915–1944, doi:10.1111/jace.17680.
- [170] T. Han, N. Stone-Weiss, A. Goel, J. Huang, A. Kumar, Machine learning as a tool to design glasses with controlled dissolution for healthcare applications, Acta Biomater. 107 (2020) 286–298, doi:10.1016/j.actbio.2020.02.037.
- [171] Y. Zhang, A. Li, B. Deng, K.K. Hughes, Data-driven predictive models for chemical durability of oxide glass under different chemical conditions, NPJ Mater. Degrad. 4 (2020) 14, doi:10.1038/s41529-020-0118-x.
- [172] N.M. Anoop Krishnan, S. Mangalathu, M.M. Smedskjaer, A. Tandia, H. Burton, M Bauchy, Predicting the dissolution kinetics of silicate glasses using machine learning, J. NonCryst. Solids 487 (2018) 37–45, doi:10.1016/j.jnoncrysol.2018. 02.023.